Geophysical investigation of the ground fissures and ground subsidence near Karla lake (Eastern Thessaly basin, Greece)

John D. Alexopoulos[1], Spyridon Dilalos[1], Serafim E. Poulos[2], Ioannis-Konstantinos Giannopoulos[1], Vasileios Gkosios[1]

[1] National and Kapodistrian University of Athens, Department of Geology and Geoenvironment, Geophysical laboratory, Panepistiomioupoli Zografou, Greece

[2] National and Kapodistrian University of Athens, Department of Geology and Geoenvironment, Division of Geography-Climatology, Panepistiomioupoli Zografou, Greece

Abstract

Ground fissures have occurred in the last four decades across the eastern Thessaly basin (Greece) resulting in damage to the villages of the area. Several studies for the area refer to the over-pumping of ground water as the main reason for their occurrence, causing sediment compaction due to the reduction of the aquifer level. In this paper, we depict the results of a joint geophysical survey trying to determine the subsurface regime of the basin and the exact reasons contributing to the existence of the ground fissures. The focal part of the survey includes gravity measurements for deeper investigation, combined with existing and already presented geoelectrical and electromagnetic data. Several borehole data have also been used for the calibration of the geophysical interpretation. The differential GNSS data of the gravity campaign revealed the ground subsidence of the area, reaching up to 9.16 meters. The alpine basement of the area is comprised mainly of metamorphic rocks, such as marbles, mica schists and gneiss-schists, covered by thick fluvioterrestrial and alluvial deposits. Several structural maps were generated in order to delineate the lateral density variations that could be related to fault zones along with the interpretive sections for geological modelling. The alpine bedrock was adumbrated in relatively great depths, with a large anticline of NW-SE direction, rising and separating the basin in two parts. In the east part, the fluvioterrestrial deposits, which are expected to play an important role in the compaction due to their water aquifer, are located only west of this anticline. At the east part, where the old lake Karla was hosted, the alluvial deposits lay directly on the alpine basement in smaller depths. This complicated regime is responsible for differential sediment compaction and the ground subsidence of the surface.

Keywords: Gravity, Vertical Electrical Soundings, Transient Electromagnetic technique, structural maps, density inversion, Euler deconvolution

1. Introduction

The catastrophic occurrence of aseismic ground fissures has been observed for the last four decades across the eastern Thessaly basin (Greece), causing differential ground subsidence and massive damage to buildings, infrastructures and roads in the local community since 1989

(Figs. 1-2). Their general direction is NW-SE (Fig. 3) and they have been impressed by several researchers (Apostolidis & Georgiou, 2007; Dimopoulou, 2012; Kaplanidis & Fountoulis, 1997, Kontogianni *et al.,* 2007; Soulios, 1997).

Figure 1: The impact of ground fissure on the structural integrity of the building.

Figure 2: A ground fissure was identified in the field in close proximity to the village of Kileler.

In general, there are several factors that may cause ground subsidence, including excessive groundwater pumping, natural compaction of unconsolidated sediments, fault movements and human activities. Differential vertical compaction of the aquifer leads to varying scales of subsidence on the terrain surface (Jachens & Holzer, 1982). There are severe implications that the ground subsidence and fissuring resulting from our study are caused by this groundwater level decline (Sidiropoulos *et al*., 2013) which is expected to cause sediment compaction as proposed by others (Kontogianni *et al.,* 2007; Soulios, 1997). Soulios (1997) connects the appearance of the ground fissures with the lower levels of the recorded aquifer levels in the area. The author also mentions that the decrease of the aquifer level even reaches 35 meters, while Apostolidis & Georgiou (2007) refer to a 60-meter decrease at the area of *Kileler*. In general, they indicate a 20-30-meter median decline for the period 1974-1994.

The differential compaction of sediments can also be triggered by the buried bedrock which is situated at shallow depths and away from the margins of a basin or by fault zones within the sediments of the basin (Burbey, 2010) or by fault-plane obstacles to groundwater flow (Holzer, 1980). Soulios (1997) believes that the orientation of the fissures is controlled by the subsurface fault zones altering the thickness of the post-alpine sediments. He also concludes that the thicker the sediments, the more significant ground subsidence. Kaplanidis & Fountoulis (1997) consider that the fissures of the central plain are connected with a fault zone of NW-SE direction.

Even though no substantial seismic activity has been recorded at the basin's plain, there are several indications from the morphotectonic analysis implying that there are geodynamic

processes still occurring (Alexopoulos *et al*., 2013). The activity is located more at the central part of the basin and not across its edges.

Several studies regarding ground deformation analysis have been published in nearby areas. Vassilopoulou *et al.* (2013) have calculated a subsidence range of 2-250 mm for the period 1992-2006 for Larissa Plain. Benekos *et al*. (2015) determined as maximum deformation rates of the ones at *Stefanovikio* and *Rizomylos* villages at 0.12-0.08 m/year and 0.07-0.04 m/y correspondingly. Argyrakis *et al.* (2020) have calculated median vertical subsidence at around 10 cm/yr during the period 2012–2017 at *Stefanovikio* village. Based on Parcharidis *et al.* (2011) an area of greatest deformation was identified to the north of *Kileler* village, reaching the value of -17.5 cm during the summer of 1998.

The outcomes of previous geophysical surveys in the area, with the contribution of other geophysical methods, including the Transient Electromagnetic Method (TEM) and Vertical Electrical Soundings (VES), have been thoroughly presented in former publications of the writers (Alexopoulos *et al*., 2013; 2017; 2019). The maximum depth of investigation was up to 200 meters, but the alpine bedrock has been revealed only at the southeast segment of the basin. For that reason, we conducted an additional set of gravity measurements in order to reach greater depths of investigation. This can be achieved by detecting local variations in the gravitational field due to the different densities of the subsurface geological feature. The denser the geological formations (e.g. alpine formations), the stronger gravitational attraction they produce. Therefore, sedimentary deposits produce weaker gravitational attraction than the alpine formations and this can be impressed by the gravity measurements. The gravity method has been effectively employed in the past for the determination of basin structure and their geotectonic regime (Ali *et al.,* 2017; de Castro *et al*., 2014; Dilalos *et al.,* 2019b; Fernandez-Cordoba *et al*., 2017; Sainz-Maza *et al.*, 2017).

2. Geological Setting

The original lake Karla was located on fine-grained sediments until 1962, when the lowest elevation of the basin is observed, at the southeastern margins of the basin. The drainage procedure of the lake was organized mainly in order to expand the agricultural land (Margaris *et al*., 2006). However, the excessive extraction of groundwater for increased agricultural purposes, has resulted in a notable decline of the groundwater level and substantial reduction in the size of the aquifer throughout the last 40 years. Taking this status into consideration, the re-construction of the artificial Karla lake (completed in 2018) was decided in order to enhance environmentally the area.

The study area is situated in the central part of mainland Greece and is practically a flat, non-symmetrical extensional, basin elongated across the axis NW-SE. It is known as the Eastern Thessaly basin, delimited by the mountains *Ossa* (north), *Mavrovouni* and *Pilion* (east) (Fig. 3). The fault systems that control the evolution of the basin and the depression of Karla lake are observed with a NW-SE direction. However, numerous dextral strikeslip tectonic structures with a WSW-ENE trend can be recognized within the peripheral area of the basin.

The alluvial deposits (*Al*) covering the basin change gradually from coarse-grained (central and western basin) to fine-grained (eastern basin), according to accessible borehole data (Sogreah Grenoble, 1974) and the geological maps. The west-southernmost zone is comprised of Neogene conglomeratic sediments, overlying the flysch (*fg*), and limestones (*Ks*). The Neogene post-alpine sediments, based on Katsikatsos *et al.* (1983), consist of unconsolidated material of clay, pebbles and sand but also fluvial-lagoonal materials, talus and scree, old talus cones and scree (*Pleistocene-Holocene*). The upper part is fluvioterrestrial formations (*Pl-Pt*), including red clays, clayey sandy material with pebbles or coarse-grained material and brecciоconglomerates, with visible thickness up to 350 meters. Their lower part is formed by lacustrine to brackish deposits (*M*), containing marls, hard marls and even travertine limestones with thickness up to 100 meters (Fig. 3).

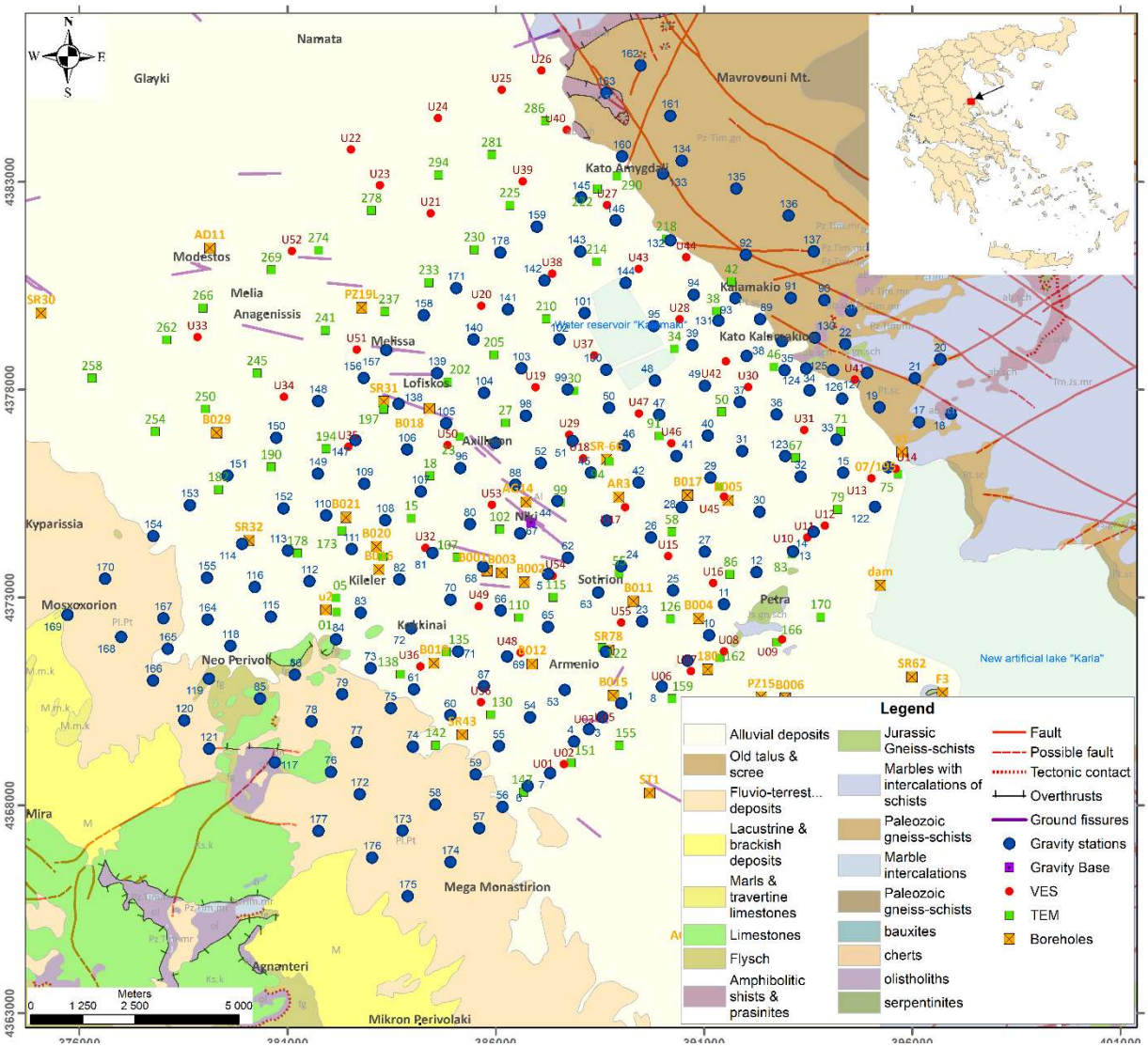

Figure 3: Compiled & simplified geological map of the basin along with the positions of the geophysical stations, boreholes and recorded ground fissures. The geological data is based on IGME maps created by Migiros & Vidakis, 1984; Katsikatsos *et al.,* 1981; 1983; 1986.

The Alpine formations examined in the eastern part of the area belong to the *Pelagoniki Unit*. At first, a Permo-triassic succession of various facies of metamorphic rocks exists (*Pz.Ti-m.gn*),

with mica schists, gneiss-schists and at the upper parts amphibolite-epidote schists, prasinites and metadiabases (Fig. 3). They alternate laterally and vertically with layers of exclusively mica schists (*Pz.Ti-m.sch.mi*) that can be found at the eastern part out of the area. These two formations overlay uncomfortably on the crystalline basement of the unit (*Pz.gn.sch*), comprised of ortho- and para-gneiss, gneiss-schists and intercalations of amphibolites. Their entire thickness can be up to 800 and 600 meters correspondingly (Migiros & Vidakis, 1984). The medium-bedded Upper Triassic-Middle Jurassic marbles (*Tm.Js.mr*) with intercalations of schists, establish the regular upward development of the aforementioned formations, with thickness up to 800 meters. In their upper parts, they are detached into plates, locally with mica schists intercalations or even with minor bauxite deposits. Overlying them, we can observe the gneiss-schists, schists (*Js.gn.sch*) with thin-bedded marble intercalations and thickness close to 200 meters. Due to an overthrust, the metamorphic ophiolitic complex (*ab.p*) can be found lying tectonically on the Upper Triassic-Middle Jurassic marbles (*Tm.Js.mr*) or the overlying gneiss-schists (*Js.gn.sch*). It comprises basic metamorphic rocks, meta-sediments and serpentinites, which can be separated into prasinites, schists and amphibolites. Its thickness can reach 500 meters. A morphological outlier (*Petra* hill) of the later geological formation (*Js.gn.sch*) can be observed, presenting steep slopes of its margins, at the interior of the basin. The alpine formations comprise marbles, metamorphic gneiss, amphibolites intercalations, schists and ophiolitic bodies (Migiros & Vidakis, 1984).

The Upper Cretaceous transgression's formations overly the Triassic-Jurassic formations or the ophiolitic complex and metasediments uncomfortably (Katsikatsos *et al.,* 1983). They consist of calcareous sandstones, pelites and pebbles of limestones or schist (*Ks*). Limestone intercalations (*Ks.k*) also exist and are mostly observed as the surficial appearance of the formation. Underlying them flysch is observed, with fine-to medium-grained sandstones, conglomerates and sandy conglomerates (*fg*). Olistoliths and even olistostromes of various lithological compositions can be investigated in the lower parts. Finally, in the study area, limestones with chert intercalations (*K6-8.k)* underlie the flysch and in our area, they are expected to be found tectonically overlying the gneiss-schists (*Js.gn.sch*)

3. Methodology

3.1 Differential GNSS data and elevation differences

Differential Global Navigation Satellite System (dGNSS) was used for the precise determination of the required coordinates of every gravity measurement. Two separate, dual-frequency antennas were used along with the establishment of a regional topographic base, according to the Hellenic Geodetic Reference System (EGSA'87) in meters. The measurements were collected using the static method, providing an accuracy of a few millimeters. The field measurements were post-processed using *TopCon Tools* software, taking into consideration the appropriate geoid corrections in order to convert the ellipsoidal heights to orthometric heights (appropriate for the gravity data reduction). During the post-processing procedure, the coordinates were also transformed into the local datum of EGSA'87. Selected geodetic benchmarks of the Hellenic Military Geographical Service in the greater area, which had not been affected by the subsidence (on the alpine formation mostly), were also re-measured with

dGNSS measurements. In that way, we managed to examine the accuracy of the coordinates' transformation especially regarding the determined orthometric heights in the EGSA'87 datum.

We detected important elevation divergences (up to -9.16 meters) between the acquired and processed dGNSS measurements (transformed in meters in EGSA'87 datum) and the older contouring derived from digitizing the topographic maps (scale 1:5000), published by the Hellenic Military Geographical Service, during the decade of 80s (Fig. 4). This phenomenon seems to be constant for the central and western basin, close to Karla lake, as illustrated with bluish colors in Figure 4. In this area, the measured elevations (with dGNSS), provide elevations lower (minus 2.5-9.16 m) than the ones of the older topographic maps. The same stands for some geodetic benchmarks of the Hellenic Military Geographical Service of the area that have been re-measured after the first results indicating the elevation difference. For that reason, we did not take into consideration the older contouring of the area but only very recent data, which keep pace with the land dGNSS measurements.

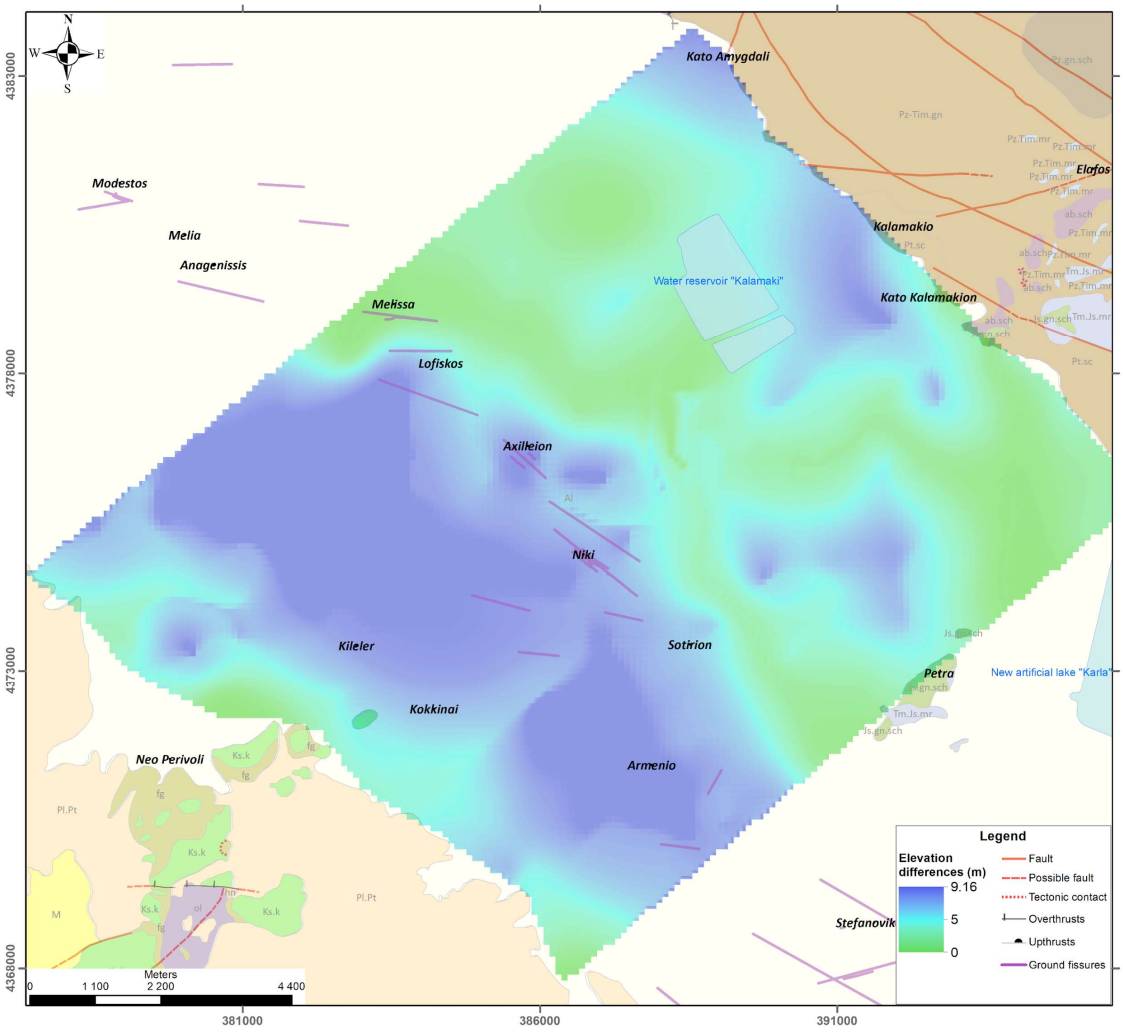

Figure 4: Elevation differences of the area between the dGNSS measurements and the topographic data by Hellenic Military Geographical Service during the decade of the 80s. The bluish colors (mainly a NW-SE zone) indicate ground subsidence, probably due to the compaction of the basin's sediments.

It is a significant subsidence of the ground surface caused most probably by the differential vertical compaction of the aquifer system during the last 40 years (1975-2015), reaching even a maximum range of 22.9 mm/yr subsidence at the area between *Kileler* and *Axilleion*. Beyond that, based on Kontogianni *et al. (*2007), an older preliminary comparison of 2005 GPS data and 1980's triangulation data also indicated elevation differences up to 3-4 meters in the Melia area.

3.2 Gravity data and processing

The gravity investigation has been conducted at the central and southern part of the eastern Thessaly basin, nearby lake Karla. The gravity measurements were arranged on a grid, with stations at roughly every 1km. The gravity database contains 179 gravity stations (Fig. 3) and an established gravity base (Easting: 386849.471, Northing: 4374799.064, Elevation: 52.162 in meters for EGSA'87). The gravity base (absolute value: 980126.528 mGal) was bound to the already established gravity base of "*Kifisia-Athens"* (Dilalos, 2018; Dilalos & Alexopoulos, 2019) and therefore is connected to the IGSN'71 datum (Morelli *et al*., 1974). The gravity data were acquired throughout the summer months using a LaCoste & Romberg G-496 gravity meter.

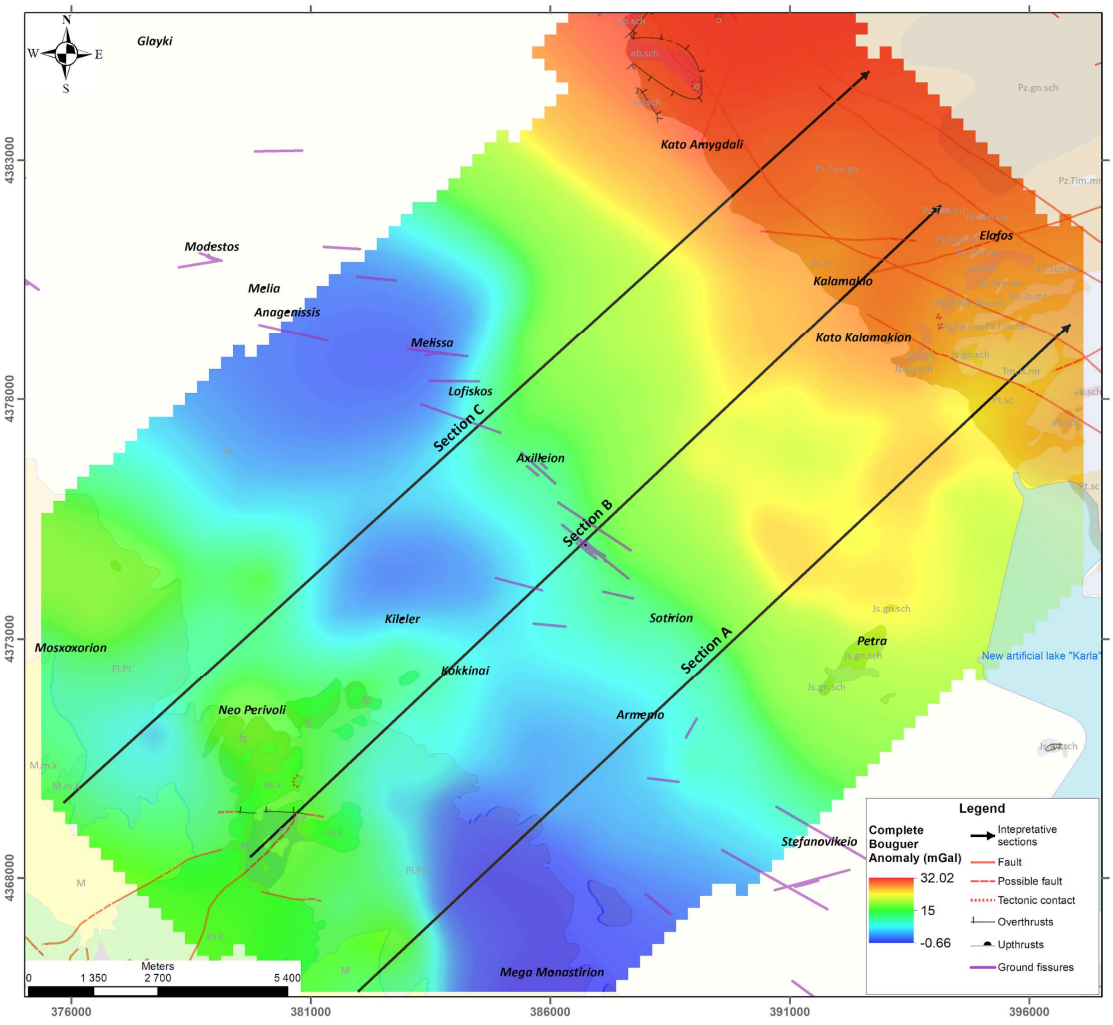

Figure 5: Complete Bouguer anomaly map of Karla basin. The locations of the profiles selected for the construction of 2.75D interpretation sections are also presented.

The *Oasis Montaj* software was utilized for the application of all the standard gravity corrections (drift, tide, latitude and free-air). The density which has been used for the Bouguer correction was 2.67 gr/cm^3, commonly used in the broader area (Dilalos & Alexopoulos, 2017; 2019; Dilalos *et al.,* 2018; Makris *et al*., 2013). Consequently, the Simple Bouguer Anomaly map has been determined. For the calculation of the terrain corrections, a Digital Elevation Model (DEM) of 5m grid spacing, based on the most recent data, has been imported to the *Gravity and Terrain Correction* component of *Oasis Montaj*, setting the internal zone up to 1.500 meters and an external one extending up to 21 kilometers. Once the terrain corrections had been applied the Complete Bouguer Anomaly Map (Fig. 5) was produced, with values from -0.67 up to 32.0 mGal. The greater values are detected primarily at the steep area in the northern area, and the lower ones in the mid part of the study area, where the basin spreads.

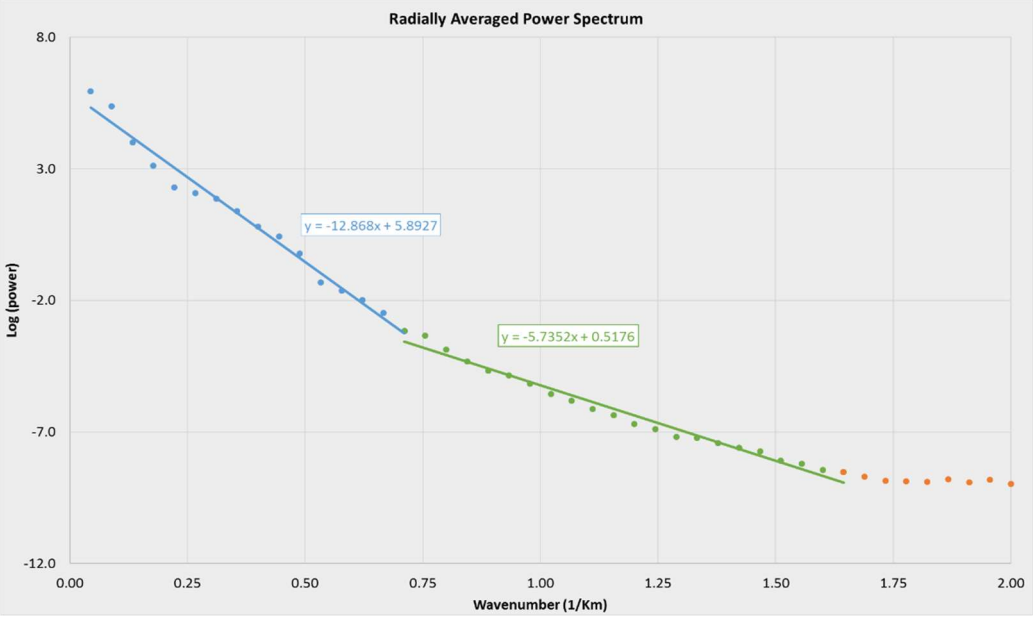

Figure 6: Radially Averaged Power Spectrum of gravity data

The next crucial step is to isolate from the Complete Bouguer Anomaly map the gravity anomalies caused by the local geological structures (residual) that we want to investigate from the deeper large-scale anomalies (regional). The procedure was implemented through the *MAGMAP* extension of Oasis Montaj (Damaceno *et al*., 2017), by applying the Gaussian filter, a smooth high-pass filter, with a cutoff wavelength of 500m. The Power Spectrum generated from the Complete Bouguer map (Fig. 5) was utilized (Dilalos *et al.,* 2019a) for the distinguishment of the residual gravity field. Two distinct depths for the anomaly sources have been recognized, at approximately 1.03 km and 0.46 km depth. Subsequently, the residual map was produced, for a standard variation of 0.44 cycles/km (Fig. 7) regarding the fairly shallow features and another residual map of the basement, for a standard variation of 0.044 cycles/km, (Fig. 8), incorporating the anomaly sources from the deeper bedrock structures. The residual map produced for the shallow anomalies (Fig. 7) has values from -1.1 mGal to 1.1 mGal. The residual map for the relatively deeper anomalies (Fig. 8) presents values from -7.76 mGal to 7.5 mGal, including the effect of all the upper structures.

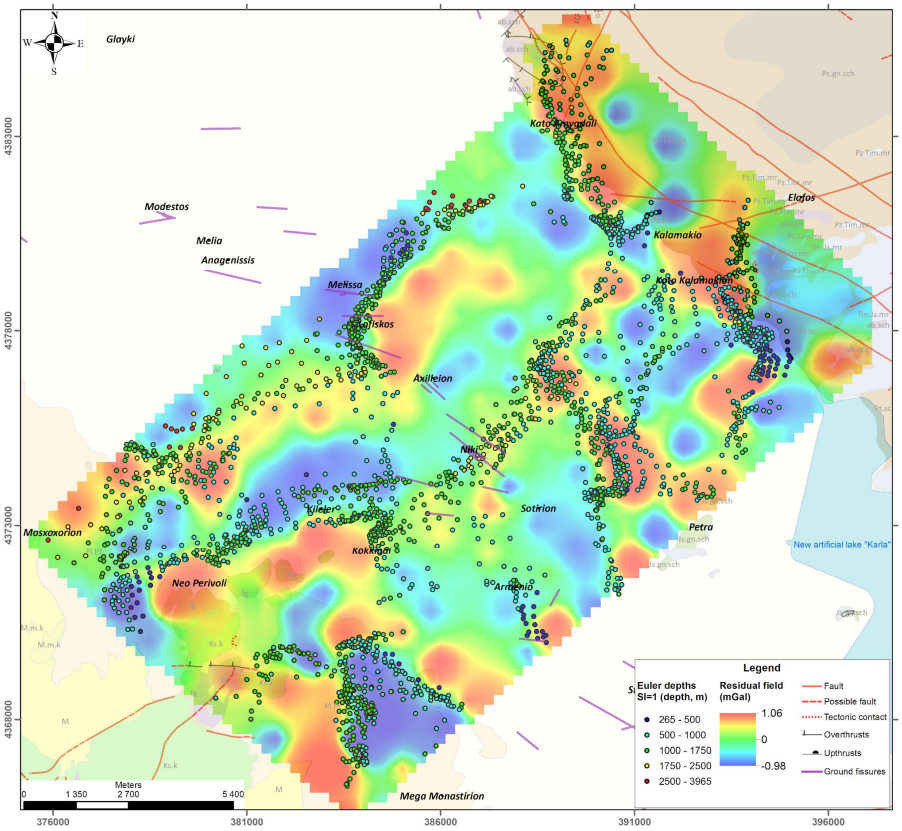

Figure 7: Residual gravity map depicting shallower features (0.44 cycles/km) alongside Standard Euler solutions (represented by graduated circles indicating depth) for SI=1.

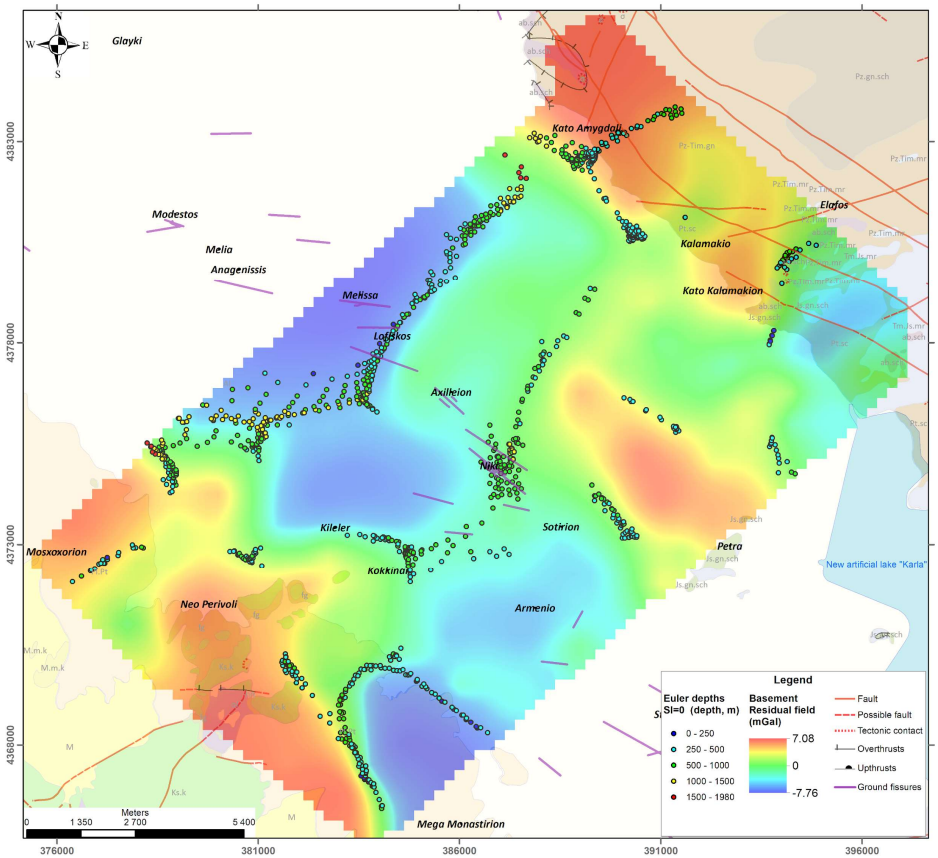

Figure 8: Residual gravity map depicting deeper features (0.044 cycles/km), alongside Standard Euler solutions (represented by graduated circles indicating depth) for SI=0.

3.3 Euler deconvolution

According to Euler's equation of homogeneity the gravity field can be related to the position, depth and data gradient of an anomaly source. During the Euler deconvolution, this source of gravity anomaly can be represented as a point mass with specific depth. These depth solutions of the Euler deconvolution are illustrated on a map, classified with their calculated depths regarding the geologic sources producing the corresponding gravity anomalies already observed, similar to various other cases (Curto *et al.,* 2015; Martins-Ferreira *et al*., 2018; Nasr *et al.,* 2011). The Euler depth solutions were determined through the *Euler3D*, for Structural Indexes (SI) zero (0) (Fig. 8) and one (1) (Fig. 7), which are considered to be the most appropriate for the adumbration of the desired fault/contact type. The selected window size of 15x15 grid points affects the accuracy of the solutions. It should not be too small because it will be prone to noise nor too high will reduce the spatial resolution. The produced solutions for Structural Index one (1) are located not only across the basin itself but also close to its marginal areas, structured either by the alpine formations (northeastern) or by the Neogene deposits (southern western). The solutions' clusters seem to form lineaments of almost NE-SW direction and fewer of NW-SE direction. They are detected in the residual map (Fig. 7), having depths mainly from 500 to 1,750 meters and a few deeper (1,750-3,965 meters) in the northern area. On the contrast, even fewer, shallower solutions (265-500 m) are located in the southern area.

As for the Structural Index zero (0), the amount of the given Euler solutions is smaller. Linear clusters of solutions have been revealed, quite restricted in swarm, in NE-SW direction and a few smaller ones in NW-SE direction. They are noted in the residual map of the basement (Fig. 8), with shallower depths, generally between 250 and 1,000 meters, but also some in greater depths (1,000-1,980 meters) at the northern zone of the basin.

3.4 Structural mapping

We benefit from the calculation of gravity derivatives that lead to the construction of structural maps. These maps practically highlight the changes of the gravity field trying to adumbrate the subsurface structural edges (e.g. faults, basin's boundaries, intrusions, salt domes), a very common and helpful approach nowadays in structural explorations (Ali *et al*., 2017; Dilalos *et al*., 2019a; Eshaghzadeh, 2015; Ghosh, 2016). The enhancement of such types of structures is essential for understanding the tectonic regime of an area, which in our case will be very useful.

The Total Horizontal Derivative (THDR), First Vertical Derivative (VDR), the Analytic Signal (AS) and the Tilt derivative are thought to be associated with the lateral alteration in the density of the geological bodies (Fairhead, 2015). To begin with, the findings of the THDR are shown in Figure 9 for the shallow anomalies or in Figure 10 for the greater depths. The highest values detect linear edges usually connected to faults and contacts. The same approach stands also for the Analytic Signal (AS) illustrated in Figures 13-14. The THDR findings for the shallow structures (Fig. 9) expose several zones, especially at the western and eastern marginals of the basin area. Their main direction is NW-SE but also NE-SW.

The outcome of the VDR is shown in Figure 11 (shallow features) and Figure 12 (deeper features). This practice is more precise for the shallow features (Fairhead, 2015). The zero crossing delineates the edge position and the highest values determine the structure setting, providing concurrent data about its negative or positive density and hence for estimating its dip. The same approach also stands for the Tilt derivative (Figs. 15-16). The negative values are eliminated in their illustrations in an attempt to handle them more easily (Dilalos *et.,* 2019a; Nasuti *et al*., 2012) by demonstrating only the uplifted features (possible horsts). The outcomes of the VDR (Figs. 11-12) imply almost equivalent edges with the ones of THDR (Figs. 9-10) but offering also evidence about the relative structure location (positive density bodies). Nonetheless, it seems that these images provide further clarification on the structural conditions, especially for the deeper structures.

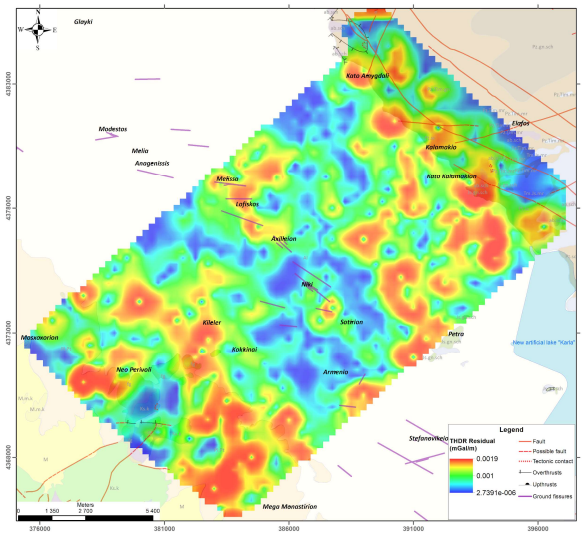

Figure 9: THDR shallow features

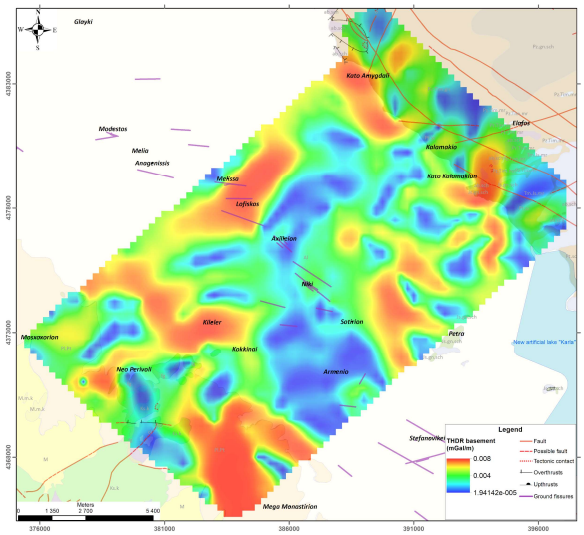

Figure 10: THDR of deeper features.

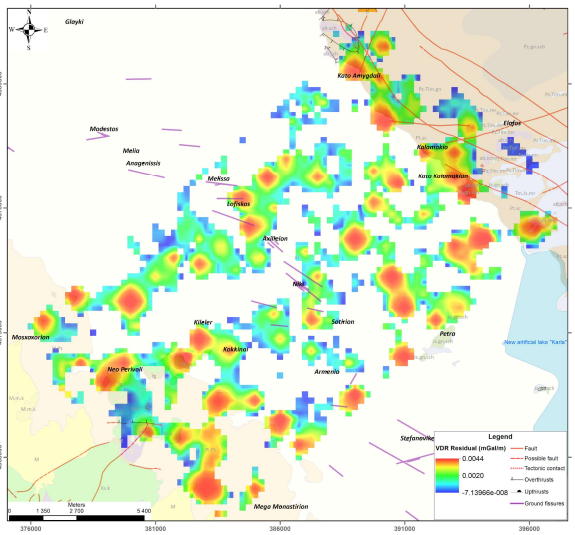

Figure 11: VDR of shallow features

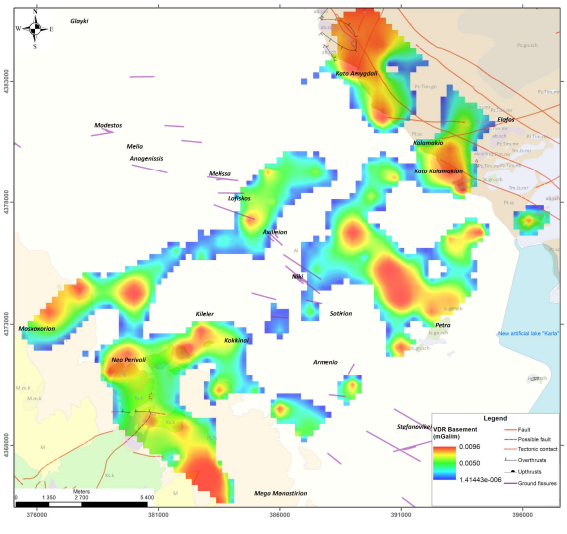

Figure 12: VDR of deeper features.

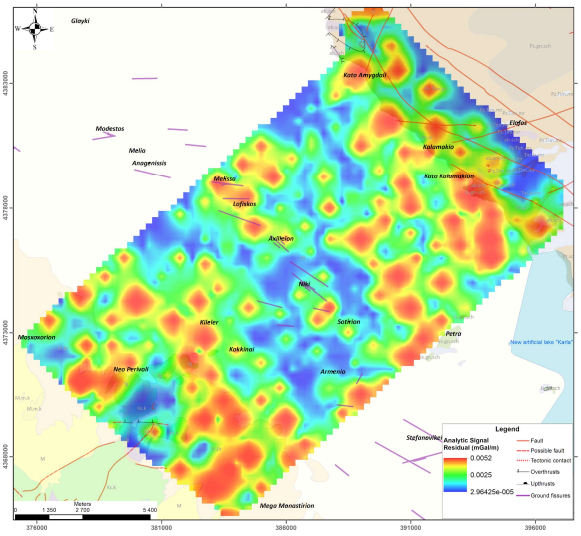

Figure 13: Analytic Signal of shallow features

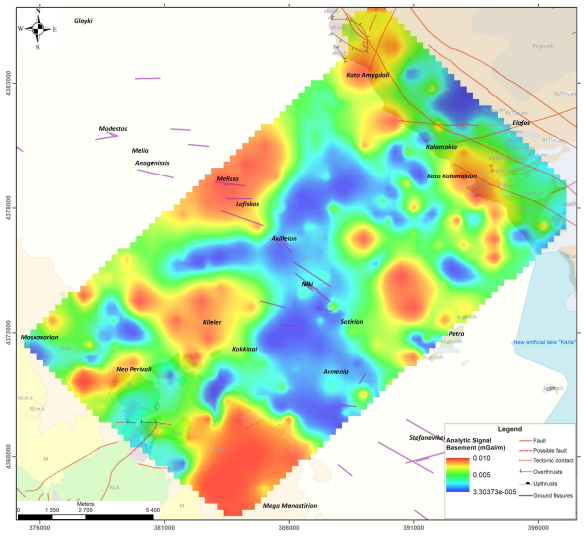

Figure 14: Analytic Signal of deeper features

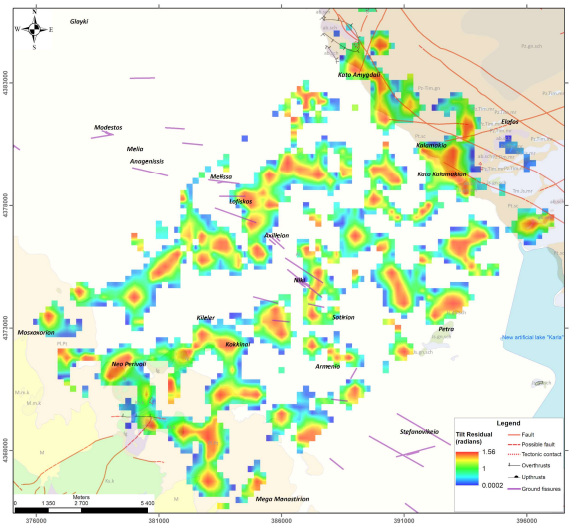

Figure 15: Tilt derivative of shallow features

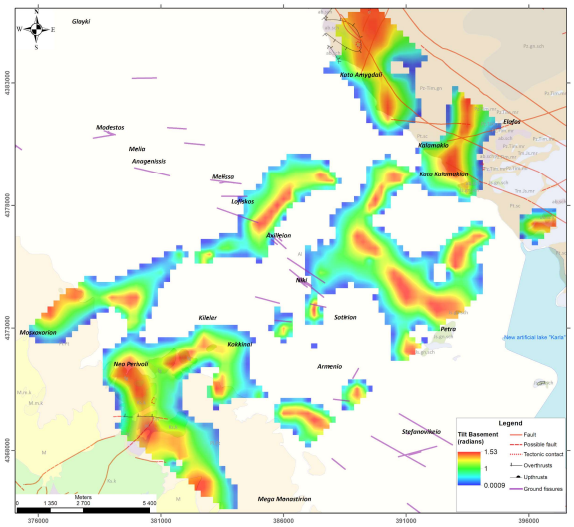

Figure 16: Tilt derivative of deeper features

3.5 3D density models

Three-dimensional gravity modelling has seen rapid development in recent years (Andersson & Malehmir, 2018; Dilalos & Alexopoulos, 2019; Farhi *et al*., 2016; Wehr *et al.*, 2018). It is a powerful technique used to reconstruct the subsurface through a three-dimensional distribution of the density. The subsurface density is directly related to the types of geological formations located in the area. Massive and compact formations have higher density values while loose formations (usually post-alpine ones) have smaller density values. Most of the time these 3D models are presented in density contrast (and not density), derived by the comparison of the calculated values with the medium density of the area.

The presented density inversions (Figs. 17-19) have been conducted using the "*VOXI*" Earth modelling component (Azizi & Saibi, 2015; Martins-Ferreira *et al*., 2018) of Oasis Montaj. We applied the unconstrained tree-dimensional gravity modelling of the residual map, with the absolute error set to 5%. At first, the subsurface was discretized in blocks with cell size of 500

meters regarding X-Y direction and 250 meters for Z. The derived block mesh contains totally 14,723 individual blocks each one with a dedicated density difference. The density contrast presents values from -0.53 gr/cm^3 (blueish colors) to 0.29 gr/cm^3 (reddish colors) up to the highest depth of almost 3,950 meters. Furthermore, an alternative pseudo-3D view is presented in Figure 17, in the form of depth slices of the inverted model (An & Di, 2016; Bersi *et al.,* 2016; Miller *et al.*, 2017) for a finer comprehension of the density distribution below the surface.

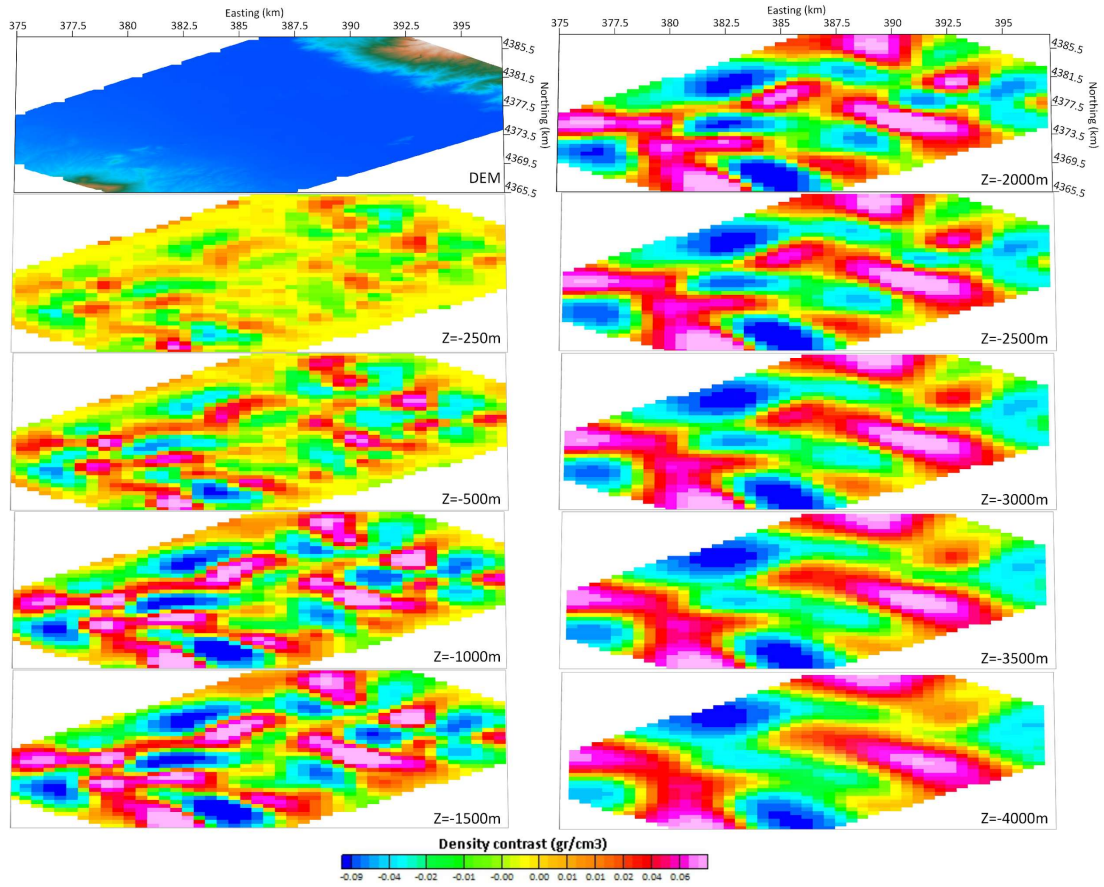

Figure 17: Depth slices derived from the three-dimensional gravity model of the Karla basin. The first figure demonstrates the area's DEM.

In Figure 18, we have separated the features with negative density contrast (values from -0.53 to -0.02 gr/cm^3) at the areas of *Mega Monastirio, Armenio, Sotirio, Kileler and Melissa* generating low gravity anomalies depicted in the residual maps (Figs. 7-8). In contrast, the features with positive density divergence (0.02-0.29 gr/cm^3) that produce high gravity anomalies, are depicted in Figure 19. They have been outlined below the areas of *Mosxoxorion, Neo Perivoli, Kato Amygdali* and *Kalamaki.*

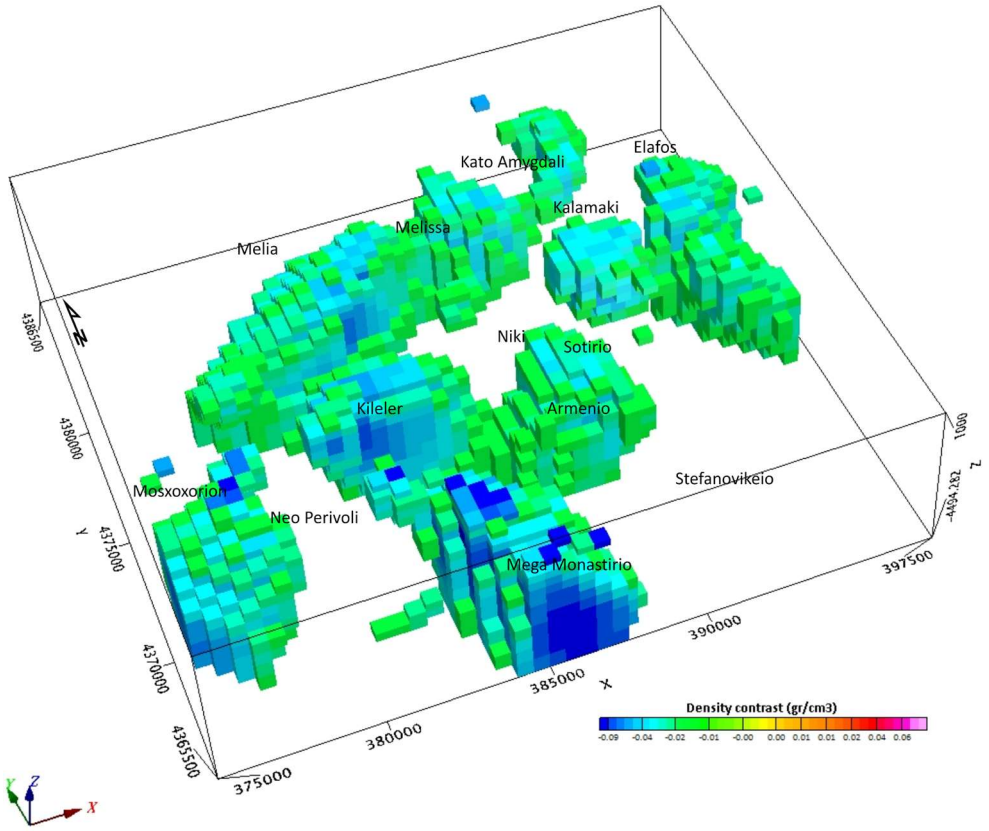

Figure 18: Three-dimensional gravity model (cell size 500m, mesh, consisting of 45x42x15 blocks), indicating features of low densities (density divergence from -0.53 to -0.02 gr/cm^3).

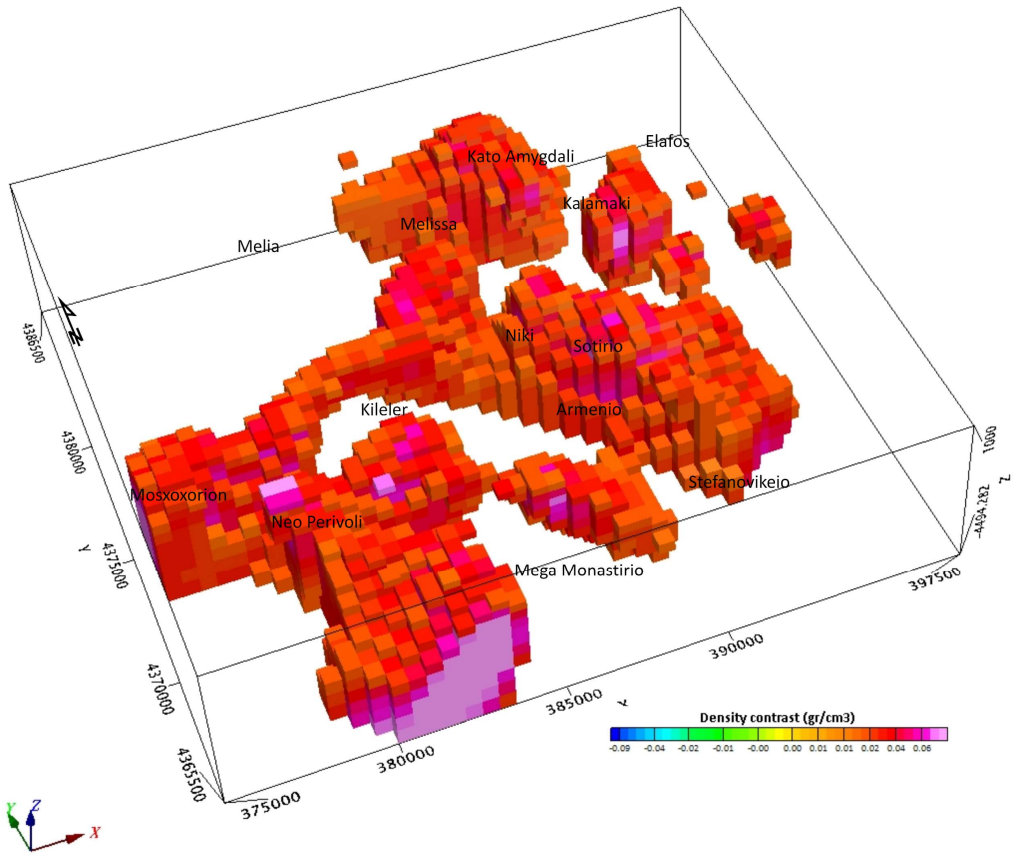

Figure 19: Three-dimensional gravity model (cell size 500m, consisting of 45x42x15 blocks), indicating features of high densities (density divergence from 0.02 to 0.29 gr/cm^3).

The outcome of the 3D models (Figs. 17-19) is quite inspiring and uncovered significant subsurface features that might prove to be a significant factor for the geotectonic regime of the East Thessaly basin. These models might be able to provide valuable insights into the characteristics (e.g., depth, throw and dip) of concealed fault zones that have not been identified in the past. Their results can be connected to the ones of the structural maps (Figs. 9-16). The areas of positive density contrast are expected to reveal the areas where the alpine bedrock is closer to the surface and the negative ones the areas with greater depths of sediments. It seems that the area has lateral alterations of the subsurface structure. The geological interpretation of the density inversions is being discussed in detail in the results and discussion section (§5), related to all other geophysical results and especially the geological-gravity sections.

3.6 Geoelectrical and Geoelectromagnetic methods

The geoelectrical technique of Vertical Electrical Soundings (VES) has been utilized effectively in the last decades for basin subsurface investigation (Al-Fares, 2016; Yadav *et al*., 2010). This method allows the investigation of quite large depths and can disclose deep geological information, by providing the vertical distribution of the electrical resistivity. Moreover, the Transient Electromagnetic Method (TEM) has been related to VES in the past for the investigation of the subsurface geological regime of post-alpine basins (Bortolozo *et al*., 2014; Mitsika et al., 2023; Porsani *et al*., 2014).

A grid of fifty-six (56) Vertical Electrical Soundings (VES) using Schlumberger array was conducted (Fig. 3), as the preliminary geophysical approach which has already been discussed (Alexopoulos *et al*., 2013; 2019). An investigation depth of 200-250 meters was reached due to the greatest current electrode spacing (AB) of 1400 m. An ABEM Terrameter System was used for the data acquisition. The geoelectrical curves were processed according to their match with the typical master and auxiliary curves for established layer parameters (Orellana & Mooney, 1966). Subsequently, the method described in Zohdy (1989), which composes a "multilayer" model was applied. After all, the Interpex IX1D was employed to generate the "layered" model based on the primary geoelectrical models determined from the graphic method by Orellana & Mooney (1966).

In addition, seventy-seven (77) TEM soundings (Fig. 3) were collected on a grid covering the investigated area and have already been discussed (Alexopoulos *et al*., 2017; 2019). The TEM soundings were conducted with ABEM's WalkTEM Time Domain Ground EM system. The field arrangement included the two in-loop antennas, RC-5 (0.5m x 0.5m) and the RC-200 (10m x 10m), along with a 40m x 40m square transmitter loop. The *ViewTEM* software was operated for the data processing and inversion providing a multi-layer resistivity model for all TEM soundings separately. Each multi-layered model was transformed into the corresponding few-layer geoelectrical model (Fig. 20), a procedure that facilitated us to interpret the TEM data.

4. Geological interpretation

4.1. Calibration of geophysical data & density determination

The geological interpretation of gravity data is guided by the density values of the explored geological formations of the area. In the context of this research, some of the density values that have been adapted originate from a recent study by the authors at the nearby deltaic area of Pineios river (Dilalos *et al.*, 2022). This is due to the fact that they share some of the geological formations and they have similar geological history. Additionally, regarding the fluvio-terrestrial quaternary sediments (*Pl.Pt*) and scree we took advantage of the calculated density values that the authors had determined from the existence of similar formation in the Athens basin (Dilalos, 2018; Dilalos *et al*., 2019a). Regarding the alluvial deposits we chose a value of 1.7 gr/cm^3 from the literature (Jacoby & Smilde, 2009; Manger, 1963), based on the lithology and the fact that they are considered dry in our case. The density values used in this study are illustrated in Table 1 and will be assigned to each prism/block during the construction of the interpretative 2.75D models.

Geological formation	**Density (gr/cm^3)**	**Resistivity (Ohm.m)**
Alluvium dry deposits (*Al*)	1.70	2-33
Fluvio-terrestrial quaternary sediments (*Pl.pt*)	2.20	19-53
Marls with travertine limestones (*M*)	2.10	-
Limestones ($K_{6\text{-}8}.k$)	2.67	-
Flysch (*fg*)	2.40	-
Marbles (*Tm.Js.mr*)	2.75	800-3,100
Mica schists (*Pz.Ti-m.sch.mi)*	2.55	110-460
Gneiss-schists (*Pz.Ti-m.gn* + *Js.sch.ph*)	2.65	45-270
Gneiss & gneiss-schists (*Pz.Tm.sch.m*)	2.75	-

Table 1: Density and resistivity values of the geological formations of the investigated area.

In a few cases, we conducted both TEM and VES soundings very close or even at the same location, revealing that their processing outcome was quite comparable. Apart from that, we also carried out some soundings close to the location of existing deep boreholes (Sogreah Grenoble, 1974; Records of Ministry of Agricultural Development and Food - Hydrology directorate and Ministry of Environment, Energy and Climate Change - Special secretariat for water) for calibration of their results (Fig. 20), proved to be valuable for the discrimination of the post-alpine sediments especially. For example, in Figure 20, the borehole data guided the interpretation of the geophysical VES and TEM data, where practically we can observe three geoelectrical layers corresponding to only one geological, the alluvial deposits. This is caused due to the alteration of the fine-grained and coarse-grained materials and has been observed for both the alluvial and the fluvio-terrestrial deposits, in several spots where we have the vicinity

of boreholes and geophysical measurements. The 1-D geoelectrical models calculated from equally the TEM and VES measurements were taken into consideration for the final interpretation of the gravity data. These two methodologies have also been used by the authors in the past (Dilalos *et al*., 2022) mostly in order to constrain the near-surface geotectonic structure of the gravity interpretation. The resistivity values of the geological formations where we have geoelectrical data, especially connected with boreholes, are presented in Table 1.

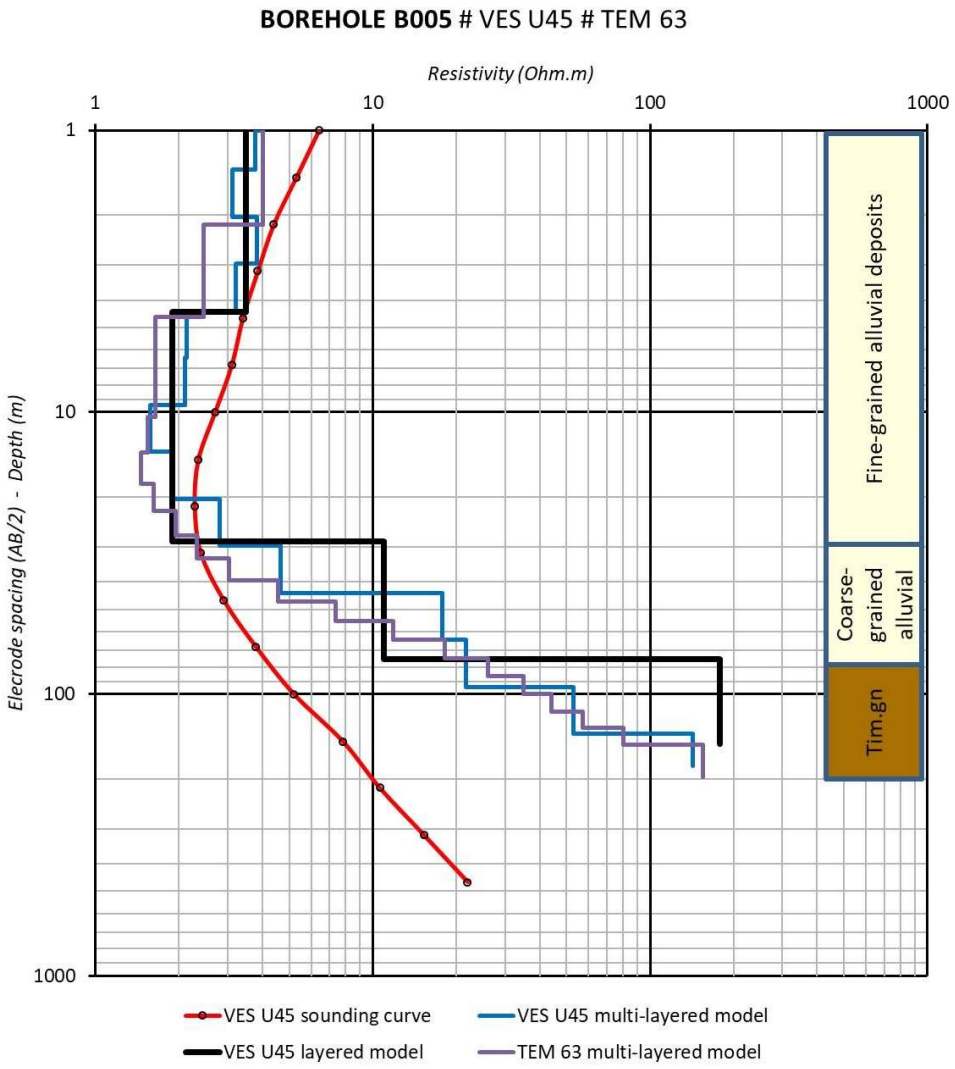

Figure 20: The geoelectrical model of VES U45, shown as a layered model (*black line*) and a multi-layer model (*blue line*), alongside the resistivity model of TEM 63 (*purple line*) but also the borehole data of B005.

4.2. 2.75D interpretative models

According to the geological regime of the investigated area and the corresponding densities of the formations, three geological-gravity sections have been structured (Fig. 21), with the support of *Geosoft* GM-SYS (Blaikie *et al.,* 2014; Kim *et al.,* 2009). The gravity response from each geological profile is estimated and associated with the observed corresponding field anomaly. The selected profiles for the production of the interpretative models are depicted in Figures 5 & 22.

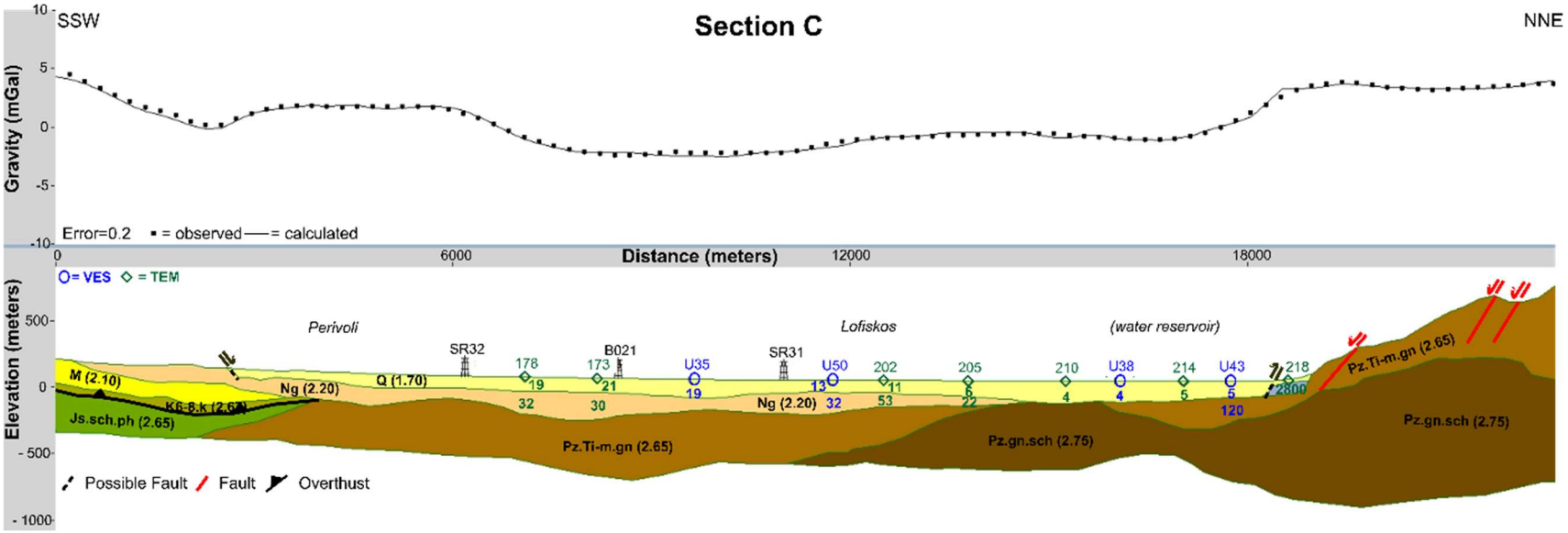
Section C
SSW
NNE
Gravity (mGal)
Error=0.2 ▪ = observed —— = calculated
Distance (meters)
O= VES ◇ = TEM
Elevation (meters)
Perivoli
Lofiskos
(water reservoir)
SR32
B021
SR31
U35
U50
U38
U43
M (2.10)
Ng (2.20)
Q (1.70)
K6-8.k (2.67)
Js.sch.ph (2.65)
Pz.Ti-m.gn (2.65)
Pz.gn.sch (2.75)
Possible Fault
Fault
Overthust

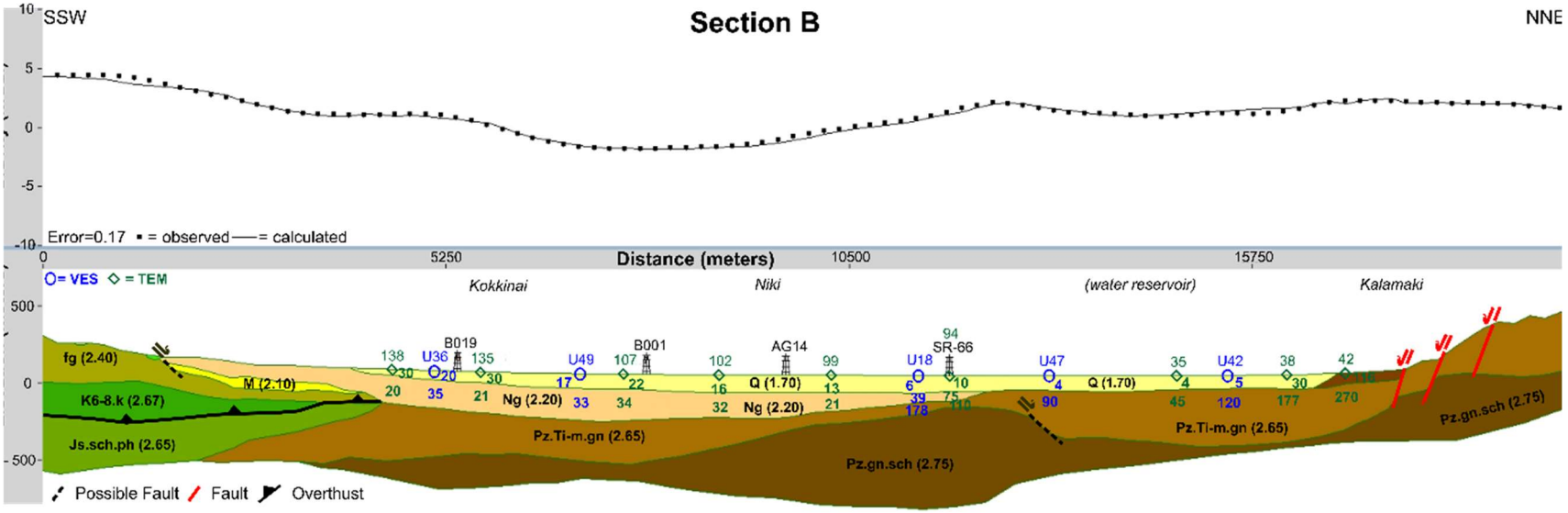
Section B
SSW
NNE
Error=0.17 ▪ = observed —— = calculated
Distance (meters)
O= VES ◇ = TEM
Kokkinai
Niki
(water reservoir)
Kalamaki
B019
B001
AG14
SR-66
U36
U49
U18
U47
U42
fg (2.40)
M (2.10)
K6-8.k (2.67)
Js.sch.ph (2.65)
Q (1.70)
Ng (2.20)
Pz.Ti-m.gn (2.65)
Pz.gn.sch (2.75)
Possible Fault
Fault
Overthust

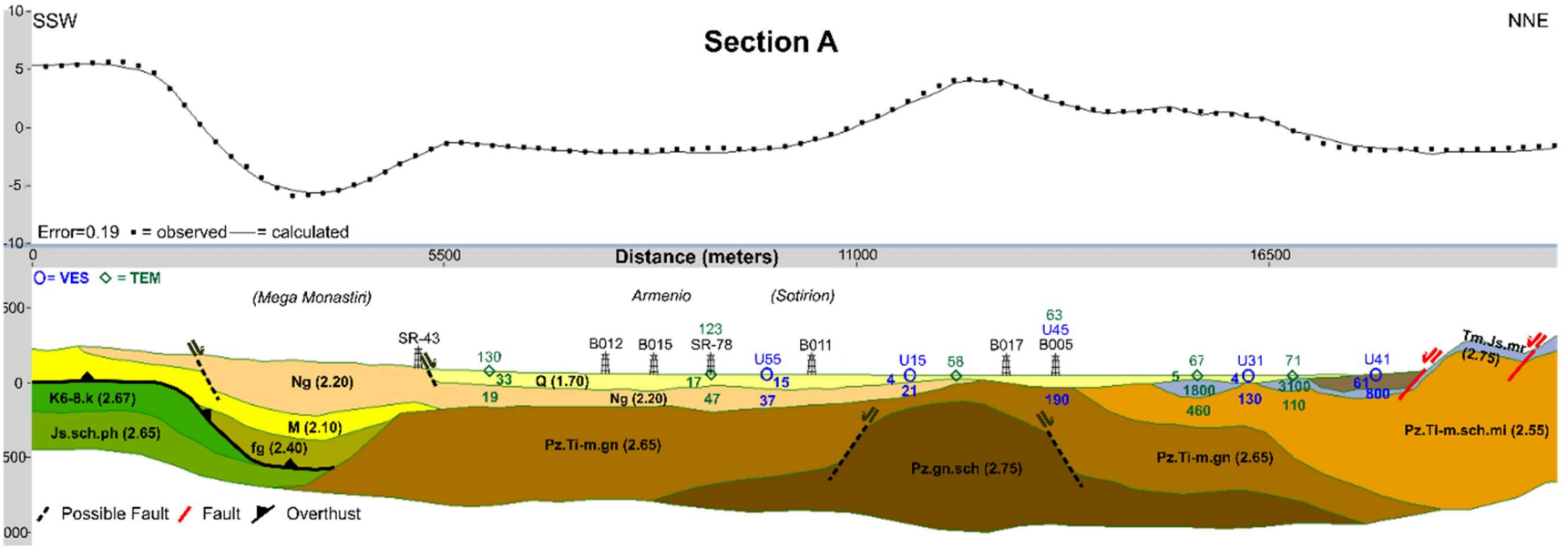

Figure 21. Gravity-geological sections (*scale 1:2*). The sections have been placed in the order of their spatial position in the area (the upper one is the northern one). The ***squares*** represent the observed residual anomaly and the ***black line*** *is* the calculated one. In the parentheses, the assigned density of the geological formations is provided. The ***blue circles*** illustrate the location of VES and the ***green rhombus*** are the corresponding TEM. Underneath them, their determined resistivity values are provided (in blue font for VES and green for TEM correspondingly). Lastly, the black drills illustrate the existing boreholes. Geological formations: ***Q***: Alluvial deposits, ***Pl.Pt***: Fluvio-terrestrial sediments, ***M***: Marls with travertine limestones, ***fg***: flysch, ***K$_{6-8}$.k***: Limestones, ***Tm.Js.mr*****:** Marbles, ***Pz.Ti-m.sch.mi*****:** Mica schists, ***Js.sch.ph*****:** Gneiss-schists ***Pz.Ti-m.gn*****:** Gneiss-schists, ***Pz.Tm.sch.m*****:** Gneiss & gneiss-schists

360

The observed residual gravity (represented with squares) is presented at the upper part of each illustration of Figure 21, alongside the calculated one (represented with a solid line) as derived from the geological model (lower part of the figures). A scale of 1:2 has been selected for the presentation (vertical exaggeration) in order to improve its understanding. The density of each block is mentioned in the brackets.

These geological models (Fig. 21) have been produced by considering all the data resulting from the geophysical measurements in the area, combined with the geological data (including the borehole ones). The interpretation profiles were based on an initial geological model inspired by the geological maps and their geological sections, the literature but also authors' personal geological recordings. The selected density values for the geological formations have been inserted as a constraint derived from the geological knowledge, guiding the computation of the gravity model response of every section. Subsequently, a procedure of correction efforts was carried out in order to improve the response and the corresponding fit of these models. The geological interpretation derived from the TEM and VES soundings was one more constraint for the geological-gravity models, targeting to the shallower depths. Finally, the constraints of the geological data from several boreholes have been considered and were probably the most crucial factor (Records of Ministry of Agricultural Development and Food - Hydrology directorate and Ministry of Environment, Energy and Climate Change - Special secretariat for water; Sogreah Grenoble, 1974)

The gravity data processing results of the 3D inversion have also been considered, providing insights to greater depths. On the contrary, VES and TEM soundings provided shallower information, as we have already mentioned (up to 250 meters). Their geological interpretation is based on their defined layered models (Alexopoulos *et al*., 2013; 2017; 2019) along with some re-processing, guided by the borehole data. This information was utilized to control and calibrate the final gravity interpretation (Dilalos *et al*., 2022; García-Pérez *et al*., 2018). Beyond that, the evaluation of the structural maps revealing the existence of possible structural edges has also been considered during the construction of the interpretative results.

5. Results and Discussion

The alluvial deposits and their thickness have been outlined across all three sections, with the greater thickness located at the north-west area. In the first half part of all interpretative sections (Fig. 21) the bottom of the alluvial deposits also represents the roof of the underlying fluvio-terrestrial sediments, which have been investigated only at the west-central part of the basin. Across the second half part of these sections, the alluvial deposits lay directly on the alpine geological formations of the *Pelagoniki* unit. On the contrary, at the beginning of all three sections, the fluvio-terrestrial sediments (*Pl.Pt*) are expected to overlay on the marls with travertine limestones (*M*). The Paleozoic metamorphic formations (marbles, schists, gneiss-schists, etc.) are found situated in relatively smaller depths as we move to the northern parts, especially the lower formation of gneiss & gneiss-schists (*Pz.Tm.sch.m*). The impression of submerging of the whole metamorphic system to the south is given, leading to the greater thickness of gneiss-schists (*Pz.Ti-m.gn*) and the appearance of mica schists (*Pz.Ti-m.sch.mi)* at the southern part (Section A). This also is connected with the existence of marbles on *Mavrovouni Mt*. in the southern part of the mountain.

The structural maps produced by the gravity data provide a qualitative evaluation that usually aids in the identification of possible concealed fault zones in the study area (Fig. 22). These originate from the lateral density contrasts produced by the different geological formations (density variation), usually observed in cases of fault zones. By combining the results of the structural maps with the subsurface structure obtained from the interpretative sections (Fig. 22), we could say that certain structural edges probably correspond to lateral sides of large-scale bedrock folds also and not faults. Such geological patterns can also produce important lateral density variations. Several other edges that have been revealed by the structural maps have been evaluated as possible faults (pink dashed lines in Fig. 22) taking into account the interpretative sections (Fig. 21) but also the paleo-relief of the basin as represented by the elevation of the roof of the alpine basement formations (Fig. 22).

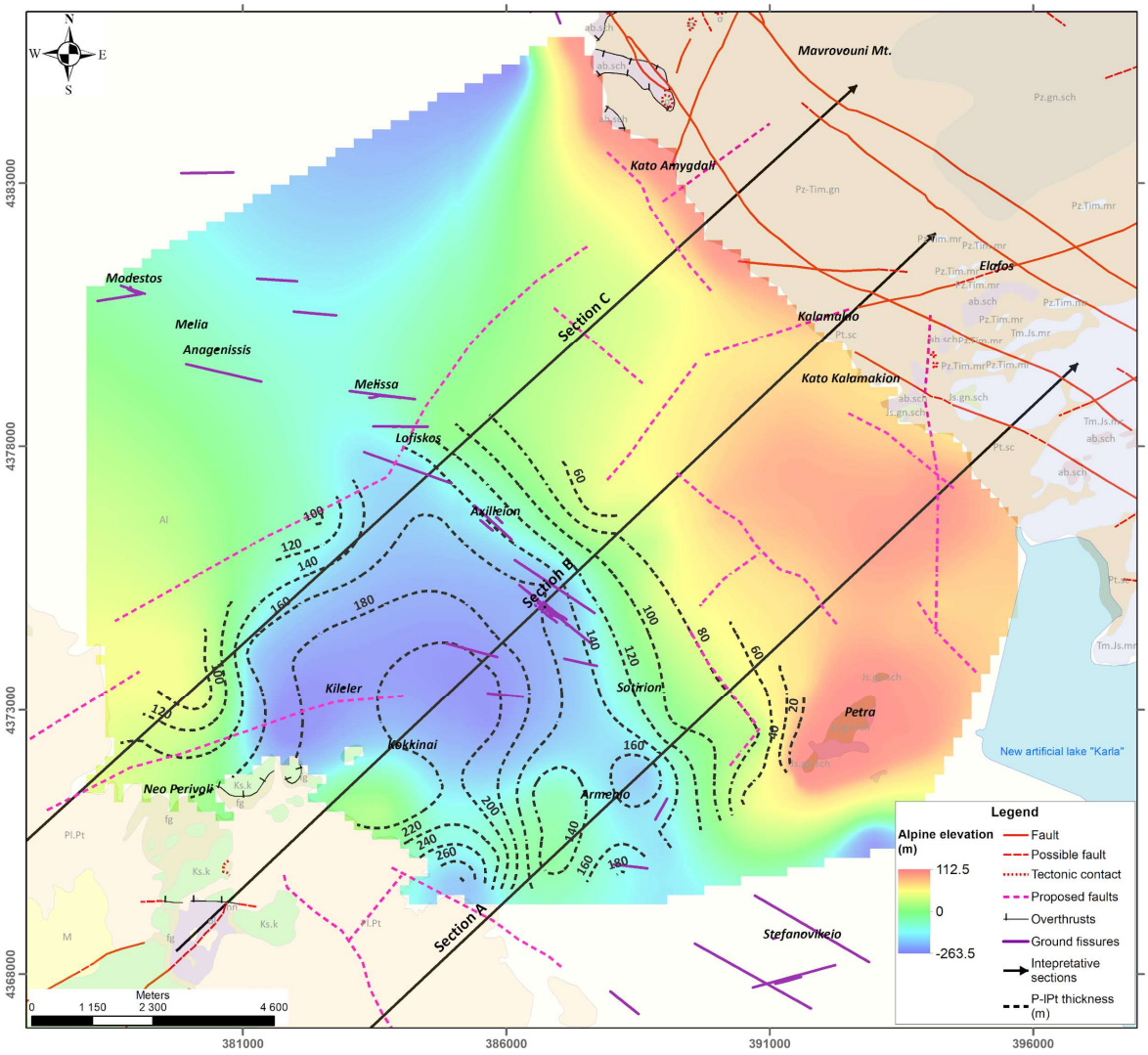

Figure 22: The elevation of the alpine's roof depicted by the color map, based on geophysical interpretation. the thickness of the fluvio-terrestrial sediments (*Pl.Pt*) can be observed with the black dashed contours. Finally, the location of the proposed fault zones derived from the structural maps is presented with pink dashed lines.

The reason that we chose to interpret some of the structural edges as the side effects of the bedrock's folding was grounded in the geological history of the area and the existing geological

sections in the geological maps. The metamorphic rocks of the *Pelagoniki* unit, including the marbles (*Tm.Js.mr*), the gneiss-schists (*Pz.Ti-m.gn*), the mica schists (*Pz.Ti-m.sch.mi*) and the crystalline basement of the unit (*Pz.gn.sch*) are presented folded. Therefore, we can spot a main anticline of the crystalline basement at the midway of all three sections. This anticline seems to control the extension of the fluvio-terrestrial, post-alpine sediments (*Pl.Pt*), since we observe that they have not been identified beyond this structure (moving towards the *Mavrovouni Mt.*). This can also be verified by the thickness of the fluvio-terrestrial sediments across the basin, as presented in contours in Figure 22, where we can also associate their absence at the northern part with a possible fault zone, revealed by the structural maps. Beyond that, their thickness seems to correlate with the depth of the alpine basement (Fig. 22), which is located in greater depths (smaller elevations) at this part of the basin. The deeper we find the alpine basement, the thicker the fluvio-terrestrial sediments.

Most of the aforementioned fault zones and folds have also been adumbrated by the 3D density models (Figs. 17-19). Correlating the features of high density, depicted in Figure 19, with the interpretative sections (Fig. 21) we could say that we can observe the three-dimensional representation of the paleo-relief of the area, composed of the crystalline basement of the unit (*Pz.gn.sch*) at the eastern area and the carbonate formations at the western. The main anticline of the crystalline basement presented in Figure 21 is also obvious in Figure 19, where the high-density formations below *Sotirio* seem to be shallower. Additionally, the existence of low-density formations across the zone *Kileler -Armenio - Mega Monastiri* and (Fig. 18) correspond to the great thickness of post -alpine formations at the area, also depicted in the interpretative sections (Fig. 21).

The geological interpretation derived from the layered models of the TEM and VES soundings proved to be extremely helpful ,especially for the calibration of the gravity interpretation regarding the shallower post-alpine deposits. Of course, the contribution of the boreholes was also crucial for the corresponding calibration of the resistivity values, mainly for sorting ~~of~~ the post-alpine sediments, having similar resistivity values. Their combined interpretation indicated that the alluvial deposits (*Al*) have been investigated with resistivity values 4-33 Ohm.m and the fluvio-terrestrial deposits (*Pl.Pt*) with 19-53 Ohm.m. More specifically, the alluvium deposits have resistivity values of 4-5 Ohm.m., at the eastern basin, where the initial Karla lake was hosted, derived from their fine-grained and highly clayey materials. Furthermore, we managed to discriminate the alpine formations of similar density, such as the marbles (*Tm.Js.mr*) with higher resistivities (800-1,300 Ohm.m) and the gneiss-schists (*Pz.Ti-m.gn*) with lower resistivities (45-270 Ohm.m). Unfortunately, the deeper alpine formation of gneiss & gneiss-schists (*Pz.gn.sch*) has not been investigated by the VES or TEM sounding, due to its great depth.

Based on the combined geophysical interpretation we have investigated the subsurface geological formations with the following the maximum thickness:

- Alluvial dry deposits (*Al*): up to 160 meters.
- Fluvio-terrestrial quaternary sediments (*Pl.Pt*): up to 360 meters,
- Marls with travertine limestones (*M*): up to 190 meters.
- Marbles (*Tm.Js.mr*): up to 120 meters.

- Mica schists (*Pz.Ti-m.sch.mi)*: up to 1020 meters.
- Gneiss-schists (*Pz.Ti-m.gn*): up to 640 meters.
- Gneiss & gneiss-schists (*Pz.gn.sch*): up to 1040 meters.

The quantitative determination of the sediment compaction (6.2-22.9 cm/yr) derived from the acquired dGNSS data during the gravity campaign, reveals the consequences of the overpumping of the area, combined with the subsurface complex geological structure. The ground subsidence that has been spotted (Fig. 4) can be justified by the geological structure proposed in our interpretative sections (Fig. 21) and is practically one of the most important parameters for the existence of ground fissures. As we can see in Figure 3, the fissures are located at the central segment of the study area, near the villages, with a general NW-SE direction. Other ground fissures have been reported across the lowland close to the villages but have not been recorded since they are usually eliminated from the tillage and the fact that there is no infrastructure to cause permanent damage. The fluvio-terrestrial sediments, as already mentioned, are located only in the western and central parts of the basin. Their eastern boundary, based on the interpretative sections, is practically determined by the main anticline of the alpine bedrock, due to its large-scale folding, also located in direction NW-SE. The fact that the alpine basement rises closer to the surface can explain the almost null elevation differences (Fig. 4) at the eastern part of the basin.

At this point, it should be reminded that the fluvio-terrestrial sediments (*Pl.Pt*) are basically composed of conglomerates and marl alternations. The conglomerates of the fluvio-terrestrial sediments hosted the main portion of the basin's subsurface water storage, but now are drained due to the overpumping, leading to their compaction and subsequently to ground subsidence of the area, up to 9.16 meters in the last 40 years. This phenomenon is examined only across the areas where we have the fluvio-terrestrial deposits underlying the alluvial deposits. That area seems to subside almost uniformly and continuously due to the continuous reduction of the aquifer level. Similar cases of ground subsidence due to overpumping have been discussed in the literature for other basins (Figueroa-Vega, 1984; Raspini *et al.*, 2014; Slaff, 1993; Sneed *et al.,* 2013).

On the other hand, the alpine bedrock cannot be affected when the aquifer is reduced, explaining the absence of ground subsidence. Therefore, we practically have an area with differential ground subsidence, since the fluvio-terrestrial deposits are restricted only to the western part of the basin. This zone of differential ground subsidence is situated across the direction of the ground fissures, affected by the paleo-relief of the alpine basement and the direction of the aforementioned alpine anticline. Maybe the concealed faults that have been exposed from the geophysical survey (Figs. 21-22) also control the location and occurrence of the ground fissures, as proposed by other researchers (Kaplanidis & Fountoulis, 1997; Kontogianni *et al.,* 2007; Soulios, 1997), even though they had not revealed them at that time. The existence of fault zones at the eastern margin may justify the minor ground subsidence calculated in these parts of the basin.

5 Conclusions

The contribution of a combined geophysical survey, including gravity, geoelectrical and geoelectromagnetic data, proved to be quite effective as we have gained new critical knowledge regarding the geological and tectonic status of East Thessaly basin, nearby lake Karla, allowing us to explain the existence of ground fissures. It highlights the importance of the integrated geophysical and geological research for the understanding of surface and subsurface dynamics, associated with hazardous phenomena, such as ground fissures and ground subsidence.

The significance of the present study lies in the fact that the geophysical investigation and mostly the gravity survey allowed us to delineate the deeper and complex geological regime of the area, revealing for example fault zones and anticline structures. The alpine bedrock of the investigated area was successfully adumbrated by taking advantage of the different physical properties of the geological formations, investigated with each method and especially the density for the gravity method. The calibration/combination of the geophysical data with several existing borehole data was crucial for the appropriate discretization of the geological formations in order to overcome the non-uniqueness of the geophysical data.

The dGNSS data acquired during the gravity campaign provided clear and quantitative evidence of the ground subsidence in the area, ranging from 6.2 to 22.9 cm/yr along a specific zone. On the other hand, the findings from the geophysical processing and their interpretation linked the main area of the ground subsidence (western and central basin) to the existence of the fluvio-terrestrial deposits and their compaction from the gradual reduction of the aquifer level. The eastern part of the area does not have sediment compaction since the alpine bedrock is underlying directly below the alluvium deposits. The reason for the elevation differences measured in the southern part of that area is probably due to faults across the alpine bedrock.

Based on all the above data the ground subsidence that causes infrastructure damage across the area is probably a combination of more than one factors. More specifically, the sediment compaction of the post-alpine sediments occurs due to the overexploitation of the groundwater needed for increased agricultural production. These two factors are also associated and probably connected with deeper fault zones and folds.

6 Acknowledgments

The field campaigns of the project were funded by the Special Account for Research Grants of NKUA contract numbers 9987, 11643, 11884 and 13504. The authors would like to thank Dr. Vassilakis Emm. for his kind provision of geological data and the geological discussions. The authors would also like to thank Dr. Mavroulis S., Mitsika G., Kalampoki E., Kaplanidi H., Farangitakis P., Doxa C., Mouliakou E., Fylaktos C and Sigala A. for their valuable contribution during the field work campaigns.

7 References

Alexopoulos, J., Vassilakis, E., Dilalos, S., Pantelis, C., Papadopoulos, T., 2013. Identification of buried active structures with preliminary geophysical and morphotectonic analysis, at eastern Thessaly basin, Greece. In: *4th International INQUA Meeting on Paleoseismology,*

Active Tectonics and Archeoseismology (Eds. Grützner C., Rudersdorf A., Pérez-López R., Reicherter K.), 9-14, Aachen, Germany.

Alexopoulos, J.D., Dilalos, S., Mitsika, G.S., 2017. Preliminary results of the application of Transient Electromagnetic Method in the area of Karla lake (East Thessaly basin, Greece). In: *Proceedings of 11th International Hydrogeological Congress*, 2, 103-112, Athens, Greece.

Alexopoulos, J., Dilalos, S., Mitsika, G.S., Vassilakis, E., Poulos, S.E., 2019. A geophysical approach to the phenomenon of ground fissures at the East Thessaly basin (Greece). In: *Near Surface Geoscience 2019 - 25th European Meeting of Environmental and Engineering Geophysics,* 1-5. European Association of Geoscientists & Engineers. https://doi.org/10.3997/2214-4609.201902379

Al-Fares, W., 2016. Using vertical electrical soundings for characterizing hydrogeological and tectonic settings in Deir El-Adas Area, Yarmouk Basin, Syria. *Acta Geophysica*, 64, 610-632. https://doi.org/10.1515/acgeo-2016-0025

Ali, M.Y., Fairhead, J.D., Green, C.M., Noufal, A., 2017. Basement structure of the United Arab Emirates derived from an analysis of regional gravity and aeromagnetic database. *Tectonophysics*, 712-713, 503-522. https://doi.org/10.1016/j.tecto.2017.06.006

An, Z . & Di, Q., 2016. Investigation of geological structures with a view to HLRW disposal, as revealed through 3D inversion of aeromagnetic and gravity data and the results of CSAMT exploration. *Journal of Applied Geophysics*, 135, 204-211. https://doi.org/10.1016/j.jappgeo.2016.10.013

Andersson, M. & Malehmir, A., 2018. Internal architecture of the Alnö alkaline and carbonatite complex (central Sweden) revealed using 3D models of gravity and magnetic data. *Tectonophysics*, 740-741, 53-71. https://doi.org/10.1016/j.tecto.2018.05.008

Anudu, G.K., Stephenson, R.A., Macdonald, D.I., Oakey, G.N., 2016. Geological features of the northeastern Canadian Arctic margin revealed from analysis of potential field data. *Tectonophysics*, 691, 48-64. https://doi.org/10.1016/j.tecto.2016.03.025

Apostolidis, E. & Georgiou, C., 2007. Technical-geological investigation of surface ground fissures at areas of Thessaly. Recording, impression and documentation. *Technical report IGME*, 128p. (*in Greek*).

Argyrakis, P., Ganas, A., Valkaniotis, S., Tsioumas, V., Sagias, N., Psiloglou, B., 2020. Anthropogenically induced subsidence in Thessaly, central Greece: new evidence from GNSS data. *Natural Hazards*, 102(1), 179-200. https://doi.org/10.1007/s11069-020-03917-w

Azizi, M. & Saibi, H., 2015. Integrating gravity data with remotely sensed data for structural investigation of the Aynak-Logar Valley, eastern Afghanistan, and the surrounding area. *IEEE Journal of Selected Topics in Applied Earth Observations and Remote Sensing*, 8(2), 816-824. Doi: 10.1109/JSTARS.2014.2347375

Benekos, G., Derdelakos, K., Bountzouklis, Ch., Parcharidis, I., 2015. Monitoring the subsidence in the plain of south Thessaly with SAR inteferometry. In: *10th International Congress of Hellenic Geographical Society*, 1313-1321. 22-24 October 2014, Thessaloniki, Greece

Bersi, M., Saibi, H., Chabou, M.C., 2016. Aerogravity and remote sensing observations of an iron deposit in Gara Djebilet, southwestern Algeria. *Journal of African Earth Sciences*, 116, 134-150. https://doi.org/10.1016/j.jafrearsci.2016.01.004

578 Blaikie, T.N., Ailleres, L., Betts, P.G., Cas, R.A.F., 2014. Interpreting subsurface volcanic
579 structures using geologically constrained 3-D gravity inversions: examples of maar-diatremes,
580 Newer Volcanics Province, southeastern Australia. Jo*urnal of Geophysical Research: Solid*
581 *Earth*, 119(4), 3857-3878. https://doi.org/10.1002/2013JB010751
582 Bortolozo, C.A., Couto Jr, M.A., Porsani, J.L., Almeida, E.R., Santos, F.A.M., 2014.
583 Geoelectrical characterization using joint inversion of VES/TEM data: A case study in Paraná
584 Sedimentary Basin, São Paulo State, Brazil. *Journal of Applied Geophysics*, 111, 33-46.
585 https://doi.org/10.1016/j.jappgeo.2014.09.009
586 Burbey, T.J., 2010 Mechanisms for earth fissure formation in heavily pumped basins,
587 Proceedings of the Eighth International Symposium on Land Subsidence, Querétaro, Mexico,
588 17–22 October. *International Association of Hydrological Sciences*, Publication 339, 3-8.
589 Curto, J.B., Vidotti, R.M., Blakely, R.J., Fuck, R.A., 2015. Crustal framework of the northwest
590 Paraná Basin, Brazil: Insights from joint modeling of magnetic and gravity data.
591 *Tectonophysics*, 655, 58-72. http://dx.doi.org/10.1016/j.tecto.2015.05.011
592 Damaceno, J.G., de Castro, D.L., Valcácio, S.N., Souza, Z.S., 2017. Magnetic and gravity
593 modeling of a Paleogene diabase plug in Northeast Brazil. *Journal of Applied Geophysics*, 136,
594 219-230. https://doi.org/10.1016/j.jappgeo.2016.11.006
595 de Castro, D.L., Fuck ,R.A., Phillips, J.D., Vidotti, R.M., Bezerra, F.H., Dantas, E.L., 2014.
596 Crustal structure beneath the Paleozoic Parnaíba Basin revealed by airborne gravity and
597 magnetic data, Brazil. *Tectonophysics*, 614, 128-145.
598 https://doi.org/10.1016/j.tecto.2013.12.009
599 Dilalos, S., 2018. Application of geophysical technique to the investigation of tectonic
600 structures in urban and suburban environments. A case study in Athens basin. *Ph.D. Thesis*,
601 National and Kapodistrian University of Athens, 321p. Athens, Greece. Doi:
602 10.12681/eadd/48791
603 Dilalos, S. & Alexopoulos, J.D., 2017. Indications of correlation between gravity
604 measurements and isoseismal maps. A case study of Athens basin (Greece). *Journal of Applied*
605 *Geophysics*, 140, 62-74. https://doi.org/10.1016/j.jappgeo.2017.03.012
606 Dilalos, S. & Alexopoulos, J.D., 2019. Quantitative subsurface information of Athens basin
607 (Greece) derived from urban gravity measurements. In: *Near Surface Geoscience 2019-1st*
608 *Conference on Geophysics for Infrastructure Planning Monitoring and BIM*,
609 We_INFRA_P23. https://doi.org/10.3997/2214-4609.201902560
610 Dilalos, S., Alexopoulos, J.D., Tsatsaris, A., 2018. Calculation of Building Correction for urban
611 gravity surveys. A case study of Athens metropolis (Greece). *Journal of Applied Geophysics*.
612 159(C), 540-552. https://doi.org/10.1016/j.jappgeo.2018.09.036
613 Dilalos, S., Alexopoulos, J.D., Lozios, S., 2019a. New insights on Athens basin (Greece)
614 subsurface geological and tectonic structure, derived from urban gravity measurements.
615 *Journal of Applied Geophysics*. 167(C), 73-105. https://doi.org/10.1016/j.jappgeo.2019.04.024
616 Dilalos, S., Alexopoulos, J.D., Lozios, S., 2019b. The contribution of urban gravity survey to
617 the subsurface geological structure of the Athens basin (Greece). In: *Near Surface Geoscience*
618 *2019- 25th European Meeting of Environmental and Engineering Geophysics*, We_25_P17.
619 https://doi.org/10.3997/2214-4609.201902472
620 Dilalos, S., Alexopoulos, J.D., Vassilakis, E., Poulos, S.E., 2022. Investigation of the structural
621 control of a deltaic valley with geophysical methods. The case study of Pineios river delta

(Thessaly, Greece). *Journal of Applied Geophysics*, 202, 104652. https://doi.org/10.1016/j.jappgeo.2022.104652

Dimopoulou, M., 2012. Hydrogeological survey in the area of ground fissures in Karla East Thessaly, *M.Sc Thesis*, National and Kapodistrian University of Athens, 545p., Athens, Greece (*in Greek*). https://pergamos.lib.uoa.gr/uoa/dl/object/1320506 (Accessed on 01 July 2024)

Eshaghzadeh, A., 2015. Image edge detection of the total horizontal gradient of gravity data using the normalized tilt angle. *Geodynamic Research International Bulletin*, 3(4), 28-33.

Fairhead, J.D., 2015. *Advances in Gravity and Magnetic Processing and Interpretation*. EAGE Publications, The Netherlands, ISBN 978-94-6282-175-0

Farhi, W., Boudella, A., Saibi, H., Bounif, M.O.A., 2016. Integration of magnetic, gravity, and well data in imaging subsurface geology in the Ksar Hirane region (Laghouat, Algeria). *Journal of African Earth Sciences*, 124, 63-74. https://doi.org/10.1016/j.jafrearsci.2016.09.013

Fernandez-Cordoba, J., Zamora-Camacho, A., Espindola, J.M., 2017. Gravity Survey at the Ceboruco Volcano Area (Nayarit, Mexico): a 3-D Model of the Subsurface Structure. *Pure and Applied Geophysics*, 174(10), 3905-3918. https://doi.org/10.1007/s00024-017-1600-4

Figueroa-Vega G.E., 1984. Case History No. 9.8, Mexico, D.F., Mexico. In: *Guidebook to Studies of Land Subsidence due to Groudwater Withdrawal*, Poland J.F. (Ed.), 217 – 232, UNESCO: Paris.

Ghosh, G.K., 2016. Interpretation of Gravity Data using 3D Euler Deconvolution, Tilt Angle, Horizontal Tilt Angle and Source Edge Approximation of the North-West Himalaya. *Acta Geophysica,* 64(4), 1112-1138. https://doi.org/10.1515/acgeo-2016-0042

García-Pérez, T., Marquardt, C., Yáñez, G., Cembrano, J., Gomila, R., Santibañez, I., Maringue, J., 2018. Insights on the structural control of a Neogene forearc basin in Northern Chile: A geophysical approach. *Tectonophysics*. 736, 1-14. https://doi.org/10.1016/j.tecto.2018.04.003

Holzer, T.L., 1980. Research at the U.S. Geological Survey on faults and earth fissures associated with land subsidence. *The Engineering Geologist*, 15(3), 1-3.

Jachens, R.C. & Holzer, T.L., 1982. Differential compaction mechanism for earth fissures near Casa Grande, Arizona. *Geological Society of America Bulletin*, 93(10), 998-1012. https://doi.org/10.1130/0016-7606(1982)93<998:DCMFEF>2.0.CO;2

Jacoby W. & Smilde P.L., 2009. *Gravity Interpretation: Fundamentals and Application of Gravity Inversion and Geological Interpretation*. Springer-Verlag Berlin Heidelberg. . ISBN: 978-3-540-85328-2.

Kaplanidis A. & Fountoulis, D., 1997. Subsidence phenomena and ground fissures in Larissa, Karla basin, Greece: Their results in urban and rural environment. In: *Proceedings International Symposium on Engineering Geology and the Environment,* 1, 729–735*,* Balkema, Rotterdam.

Katsikatsos, G., Vidakis, M., Migiros G., 1981. Geological Map of Greece, scale 1:50.000, sheet Platycampos, IGME, Greece

Katsikatsos, G., Mylonakis, I., Triantaphyllidis, E., Papadeas, G., Psonis, C., 1983. Geological Map of Greece, scale 1:50.000, sheet Velestino, IGME, Greece

Katsikatsos, G., Mylonakis, I., Vidakis, M., Hecht, J., Papadeas, G., 1986. Geological Map of Greece, scale 1:50.000, sheet Volos, IGME, Greece

Kim Y.M., Lee S.M., Okino K., 2009. Comparison of gravity anomaly between mature and immature intra-oceanic subduction zones in the western Pacific. *Tectonophysics*, 474(3-4), 657-673. https://doi.org/10.1016/j.tecto.2009.05.004

Kontogianni, V., Pytharouli, S., Stiros, S., 2007. Ground subsidence, Quaternary faults and vulnerability of utilities and transportation networks in Thessaly, Greece. *Environmental Geology*, 52(6), 1085-1095. https://doi.org/10.1007/s00254-006-0548-y

Makris, J., Papoulia, J., Yegorova, T., 2013. A 3-D density model of Greece constrained by gravity and seismic data. *Geophysical Journal International*, 194(1), 1-17. https://doi.org/10.1093/gji/ggt059

Manger, G.E., 1963. Porosity and bulk density of sedimentary rocks. *Geological Survey Bulletin*, 1114(E), 60p.

Margaris, N., Galogiannis, C., Grammatikaki, M., 2006. Water management in Thessaly, central Greece, In: *Groundwater and Ecosystems* (Eds. Baba, A., Howard, K.F., Gunduz, O.), 237-242, Springer Netherlands, .

Martins-Ferreira, M.A.C., Campos, J.E.G., Von Huelsen, M.G., Neri, B.L., 2018. Paleorift structure constrained by gravity and stratigraphic data: The Statherian Araí rift case. *Tectonophysics*, 738-739, 64-82. https://doi.org/10.1016/j.tecto.2018.05.014

Migiros, G. & Vidakis, M., 1984. Geological Map of Greece, scale 1:50.000, sheet Ayia-Panayia Ayias, IGME, Greece.

Miller, C.A., Williams-Jones, G., Fournier, D., Witter, J., 2017. 3D gravity inversion and thermodynamic modelling reveal properties of shallow silicic magma reservoir beneath Laguna del Maule, Chile. *Earth and Planetary Science Letters*, 459, 14-27. https://doi.org/10.1016/j.epsl.2016.11.007

Mitsika, G.S., Alexopoulos, J.D., Vassilakis, E., Dilalos, S., Poulos, S.E., 2023. Investigation of the physical-geographical characteristics of river delta with geophysical and satellite data. The case study of Pineios River, Greece. *MethodsX*, 10, 102033. https://doi.org/10.1016/j.mex.2023.102033

Morelli, C., Gantar, C., Honkasalon, T., McConnel, K., Tanner, J.G., Szabo, B., Uotila, U., Whalen, C.T., 1974. *The International Standardization Net 1971 (IGSN71)*. IUGG-IAG Publ. Spec. 4. Int. Union of Geod. and Geophysics.

Nasuti, A., Pascal, C., Ebbing, J., 2012. Onshore–offshore potential field analysis of the Møre–Trøndelag Fault Complex and adjacent structures of Mid Norway. *Tectonophysics*, 518, 17-28. https://doi.org/10.1016/j.tecto.2011.11.003

Nasr, I.H., Amiri, A., Inoubli, M.H., Salem, A.B., Chaqui, A., Tlig, S., 2011. Structural setting of northern Tunisia insights from gravity data analysis Jendouba case study. *Pure and Applied Geophysics*, 168(10), 1835-1849. https://doi.org/10.1007/s00024-010-0189-7

Orellana, E., Mooney, H.M., 1966. *Master Tables for Vertical Electrical Soundings over Layered Structures*. Interciencia, Madrid

Parcharidis, I., Foumelis, M., Katsafados, P., 2011. Seasonal ground deformation monitoring over Southern Larissa Plain (Central Greece) by SAR interferometry. In: *Advances in the research of aquatic* environment, 497-504. Springer, Berlin, Heidelberg. https://doi.org/10.1007/978-3-642-24076-8_58

Porsani, J.L., Leite, D.N., Bortolozo, C.A., Couto Jr., M.A., Campana, J.D.R., 2014. Geoelectrical studies by VES/TDEM joint inversion in the Paraná sedimentary basin, Brazil. In: *Near Surface Geoscience 2014-20th European Meeting of Environmental and Engineering Geophysics*, 1-5. European Association of Geoscientists & Engineers. https://doi.org/10.3997/2214-4609.20142017

Raspini, F., Loupasakis, C., Rozos, D., Adam, N., Moretti, S., 2013. Ground subsidence phenomena in the Delta municipality region (Northern Greece): Geotechnical modeling and validation with Persistent Scatterer Interferometry. *International Journal of Applied Earth Observation and Geoinformation*, 28, 78-89. http://dx.doi.org/10.1016/j.jag.2013.11.010

Sainz-Maza, S., Montesinos, F.G., Martí, J., Arnoso, J., Calvo, M., Borreguero, A., 2017. Structural interpretation of El Hierro (Canary Islands) rifts system from gravity inversion modelling. *Tectonophysics*, 712, 72-81. https://doi.org/10.1016/j.tecto.2017.05.010

Sidiropoulos, P., Mylopoulos, N. Loukas, A., 2013 Optimal Management of an Overexploited Aquifer under Climate Change: The Lake Karla Case. *Water Resources Management,* 27, 1635–1649. https://doi.org/10.1007/s11269-012-0083-4

Slaff, S., 1993. Land subsidence and earth fissures in Arizona. Arizona Geological Survey, *Down-to-Earth Series*, 3, 32 p. http://hdl.handle.net/10150/629605

Sneed M., Brandt J.T., Solt M., 2013. Land subsidence along the Delta-Mendota Canal in the northern part of the San Joaquin Valley, California, 2003-10. *Scientific Investigations Report* 2013-5142. US Geological Survey. https://doi.org/10.3133/sir20135142

Sogreah Grenoble, 1974. Development study of the subsurface water storage of Thessaly plain, *Technical Report R11971*, Ministry of Agriculture of Greece.

Soulios, G., 1997. Subsidence de terrains alluviaux dans le sud-est de la plaine de Thessalie, Grèce. In: *Proceedings International Symposium on Engineering Geology and the Environment*. Balkema, Rotterdam.

Wehr, H., Chevrot, S., Courrioux, G., Guillen, A., 2018. A three-dimensional model of the Pyrenees and their foreland basins from geological and gravimetric data. *Tectonophysics*, 734, 16-32. https://doi.org/10.1016/j.tecto.2018.03.017

Vassilopoulou, S., Sakkas, V., Wegmuller, U., Capes, R., 2013. Long term and seasonal ground deformation monitoring of Larissa Plain (Central Greece) by persistent scattering interferometry. *Open Geosciences*, 5(1), 61-76. https://doi.org/10.2478/s13533-012-0115-x

Yadav, G.S., Dasgupta, A.S., Sinha, R., Lal, T., Srivastava, K.M., Singh, S.K., 2010. Shallow sub-surface stratigraphy of interfluves inferred from vertical electric soundings in western Ganga plains, India. *Quaternary International*, 227(2), 104-115. https://doi.org/10.1016/j.quaint.2010.05.030

Zohdy, A.A., 1989. A new method for the automatic interpretation of Schlumberger and Wenner sounding curves. *Geophysics*, 54(2), 245-253. https://doi.org/10.1190/1.1442648